C. R. Mecanique 344 (2016) 296–318

Contents lists available at ScienceDirect

Comptes Rendus Mecanique

www.sciencedirect.com

Computational simulation of manufacturing processes

Ductile damage prediction in sheet and bulk metal forming

Houssem Badreddine, Carl Labergère, Khemais Saanouni *

ICD/LASMIS, STMR UMR-CNRS 6281, University of Technology of Troyes, 12, rue Marie-Curie, CS 42060, 10004 Troyes cedex, France

ARTICLE INFO

Article history:
Received 5 October 2015
Accepted 21 November 2015
Available online 2 March 2016

Keywords:
Non-associative plasticity
Anisotropic plasticity
Nonlinear hardening
Anisotropic damage
Numerical methods
Metal forming
Numerical simulation

ABSTRACT

This paper is dedicated to the presentation of an advanced 3D numerical methodology for virtual sheet and/or bulk metal forming simulation to predict the anisotropic ductile defects occurrence. First, the detailed formulation of thermodynamically-consistent fully coupled and fully anisotropic constitutive equations is given. The proposed constitutive equations account for the main material nonlinearities as the anisotropic plastic flow, the mixed isotropic and kinematic hardening and the anisotropic ductile damage under large inelastic strains. Second, the related numerical aspects required to solve the initial and boundary value problem (IBVP) are very briefly presented in the framework of the 3D finite element method. The global resolution schemes as well as the local integration schemes of the fully coupled constitutive equations are briefly discussed. Finally, some typical examples of sheet and bulk metal forming processes are numerically simulated using the proposed numerical methodology.

1. Introduction

The main objective of modern metal forming processes is to design robust and lightweight structural components which help reducing carbon dioxide emissions during both the manufacturing process as well the future use of the final product. Accordingly, the rising demands of customers concern the lightweight design in order to reduce significantly energy consumption and cost efficiency while increasing the structures' service life by enhancing their stability and deformation resistance under various thermomechanical loading paths. These objectives cannot be reached without the help of an 'efficient' and 'robust' numerical or virtual design methodology based on:

- 'advanced' constitutive equations to describe, as accurately as possible, the main thermomechanical fields and their various interactions (full coupling effects) during their evolution,
- 'advanced' numerical tools to predict robustly and accurately the evolution of the deformation processes and the possible defects occurrence during the manufacturing processes or during the use of the final component in any mechanical system.

In fact, when formed or machined by large elasto-inelastic strains under room or high temperature, metallic materials undergo a strong localization of inelastic flow which is often at the origin of the initiation, growth and coalescence of microcracks and/or microvoids usually called the ductile damage. Depending on the geometrical complexity of the forming

* Corresponding author.
E-mail address: khemais.saanouni@utt.fr (K. Saanouni).

http://dx.doi.org/10.1016/j.crme.2015.11.006

tools, which define the shape of applied loading path, this well-known mechanism of ductile fracture may cause the loss of the quality of the formed part by the formation of macroscopic cracks propagating inside this formed part. This ductile damage can be seen as a natural consequence of the large inelastic strain localization which itself is strongly dependent on the main thermomechanical phenomena such as the mixed isotropic and kinematic hardening, the heat flux, the various initial and induced anisotropies, the initial microstructure of the material and its change (texture) under the applied loading paths. Accordingly, the constitutive equations used to simulate and to optimize numerically these metal forming processes should account for these phenomena and their mutual interactions or strong coupling.

Many published works have been devoted to the optimization of bulk and sheet metal forming processes using various more or less simplified approaches. For example, in the forming of thick or thin metallic sheets, the goal is to enhance the capacity of the sheet to carry a large inelastic "homogeneous" strain without any strong localization, giving some through thickness necking prior to a macroscopic crack formation. In engineering practice, the material formability is usually assessed with strain-based forming limit diagrams (FLD) in the case of linear (or proportional) strain loading paths as pioneered by Mariciniak and coworkers [1,2]. These forming limit diagrams or curves are determined from the experimental measurement of the necking or local fracture onset under linear strain paths using the minor and major principal strain diagram. However, it has been shown [3–10] that these strain-based forming limit criteria are not efficient when the applied strain path is not linear (or is non-proportional). Unfortunately, in major forming processes, the strain paths supported by deforming material points during the deformation process have been shown to be neither linear nor monotonic. This is mainly due to the complexity of the geometry of the tools (dies, punches), which cause locally reversed strain path exhibiting non-negligible Bauschinger effects. This is clearly the case in sheet-forming processes, for which the FLD prediction underestimates the failure strain as observed in many works (see [11–16] among others). To avoid these drawbacks, some authors proposed to construct the FLD (or FLC) in the stress space instead of the strain space, leading to the so-called stress-based forming limit diagram, FLSD [3–10]. However, this approach has been shown to be not efficient for complex combined stress paths (mainly non-proportional loading paths exhibiting additional hardening), where material hardening is strongly dependent on the shape of the loading path [12,13,17]. On the other hand, when necking takes place somewhere in the sheet, the plane stress assumption, on which is based the FLSD, becomes highly questionable and the predicted local stress state is less accurate or simply wrong.

Another way, proposed in many works in order to enhance the predictivity of the forming limit curves, consists in completing the yield function, of von Mises or Hill types, by appropriate instability criteria based on the pioneering works by [18–20]. Most instability theories assume the existence of an initial imperfection with a given geometrical definition, leading to a high sensitivity to the size of such an assumed initial imperfection. On the other hand, the prediction of plastic strain and its value at the final fracture is highly dependent on the used constitutive equations and on whether or not they account for non-linear mixed isotropic and kinematic hardening as well as the ductile damage effect on plastic flow and hardening evolution. In order to avoid this problem, many authors proposed to replace the initial imperfection by using an appropriate ductile damage theory, which allows catching naturally the instability conditions due to the damage initiation without assuming the existence of any initial imperfection [21–24] among many others.

An alternative approach, proposed in the recent last two decades, to predict the localized neck prior to fracture in sheet or bulk metal forming, is the full coupling between the material's behavior and the ductile damage using either macroscopic monoscale or micro–macro multiscale modeling approaches as can be found in the recent books dedicated to the damage prediction in metal forming [25–27]. Two different kinds of damage theories are used in metal forming problems: Gurson's damage theories [28–37] (among others) and continuum damage mechanics (CDM) theories [26,27,38–74]. The equivalence between CDM and Gurson-type damage coupling has been investigated in [54], where the potentialities of the CDM approach compared to Gurson's approach have been discussed mainly concerning damage-induced anisotropy and its effect on the other fields (strong coupling). This kind of fully coupled approach accounts for the direct interactions (or strong coupling) between the inelastic flow, including different kinds of hardening, and the ductile damage initiation and growth. This full coupling allows the "natural" description of the strain localization modes inside the deformed part on the basis of the effect of the ductile damage evolution in the other mechanical fields under concern. Hence, it provides a simple and helpful way to predict where and when the inelastic flow localizes due to the earliest stage of ductile damage initiation without reference to any initial imperfection. The main advantages of this fully coupled approach are [26,27]:

- it can be used, without any limitation, with advanced constitutive equations accounting for initial and induced anisotropies described by various quadratic or non-quadratic yield functions and plastic potentials. Many physical phenomena related to large inelastic strain coupled with ductile isotropic or anisotropic damage can be taken into account;
- the effect of the loading path shape in the stress or strain space (non-proportionality) and in time (cyclic loading) is considered, including the reversibility of the load with or without compressive phase. This accounts for:
  - the Bauschinger effect (kinematic hardening),
  - the closure of microcracks and/or micro-voids (unilateral effect) under the compressive phase of the loading path and its effect on the recovery of some physical properties as the microcracks close;
- due to the localization modes giving rise to highly varying thickness, this approach will be used within full 3D or specific thick shell formulations in order to avoid the weakness related mainly to the plane stress assumption.

This kind of approach leads to thermodynamically-consistent constitutive equations (for elasticity, (visco)plasticity, mixed hardening, damage, friction, thermal exchange, environment effect ...) with material parameters having a clear intrinsic character. In fact, since each phenomenon accounted for is represented by a couple of state variables, which in turn are governed by appropriate ordinary differential equations, the identification procedure is decomposed in different steps and the material parameters are determined using an inverse numerical approach for each phenomenon while the other parameters are maintained fixed [26,27].

Note that the advanced fully adaptive numerical methodology developed by the authors is well working only in 2D cases and has been already published. Since its 3D version is still under development, this paper is dedicated to the presentation of an advanced 3D (spatially non-adaptive) numerical methodology for virtual sheet and/or bulk metal forming simulation. Section 2 gives the formulation of thermodynamically-consistent fully coupled multiphysical constitutive equations accounting for the main material nonlinearities as the large plastic flow, the isotropic and kinematic hardening, and the ductile anisotropic damage under large inelastic strains. The kinematics of the homogeneous finite transformation is briefly presented. The formulation of the constitutive equations describing the mechanical behavior of the material is described in some details based on the appropriate choices of the state and dissipation potentials. A brief extension is made to include the temperature effect including the heat exchange and viscoplasticity. Finally, some indications are given concerning the modeling of the constitutive equations for the contact/friction at the solid/tool interfaces.

Section 3 is dedicated to the related numerical aspects. First, the time and space discretization of the Initial and Boundary Value Problem (IBVP) in the framework of the finite difference method in time and the finite element method in space are discussed. The well-known static implicit (SI) and dynamic explicit (DE) global resolution schemes are summarized, followed by the detailed presentation of the local integration scheme of the fully coupled constitutive equations. The numerical treatment of the contact between deformable solids is reviewed in the framework of master/slave surface methods taking into account the friction constitutive equations. Finally, a brief description of the fully adaptive numerical methodology for virtual metal forming is presented.

Section 4 shows some application of the proposed virtual metal forming methodology to some sheet and bulk metal forming processes with damage occurrence. Finally, some conclusions and perspectives of this work are given.

Throughout this chapter the following notations are used: $x, \vec{x}, \underline{x}, \underline{\vec{x}}, \underline{\underline{x}}$ indicate the zero (scalar), first (vector), second, third and fourth rank tensors, respectively. The usual tensorial product is indicated by the symbol $\otimes$, while the contracted (or inner) product is indicated by $\cdot$, $:$, $\therefore$ and $::$ for the simple, double, triple and quadruple contractions respectively. In indicial form with respect to any orthonormal Cartesian frame of basis $\vec{e}_j$ $(\vec{e}_1, \vec{e}_2, \vec{e}_3)$, this gives: $\vec{x} \cdot \underline{y} = x_i y_{ij} = a_j \vec{e}_j = \vec{a}$, $\underline{x} : \underline{y} = x_{ijkl} y_{kl} = a_{ij} = \underline{a}$, $\underline{\vec{x}} \therefore \underline{\underline{y}} = x_{ijk} y_{ijkl} = a_l \vec{e}_l = \vec{a}$ or $\underline{\underline{x}} :: \underline{\underline{y}} = x_{ijkl} y_{ijkl} = a$.

2. Thermodynamically-consistent fully coupled constitutive equations

Here, we limit ourselves to the modeling of the nonlinear behavior of metallic materials including elasticity, (visco)plasticity, mixed hardening and ductile damage with various initial and induced anisotropies. As long as the metallic materials are concerned, the assumption of the small elastic strains and large inelastic (plastic or viscoplastic) strains is adopted.

2.1. Kinematics of finite strains

The concept of intermediate configuration using the classical multiplicative decomposition of the total gradient $\underline{F}$ into elastic $\underline{F}^e$ and plastic $\bar{\underline{F}}^p$ parts is adopted to define the elastoplastic kinematics. Accordingly, the total gradient of the homogeneous transformation is given by:

$$\underline{F} = \underline{F}^e \cdot \bar{\underline{F}}^p = \underline{Q} \cdot \bar{\underline{V}}^e \cdot \bar{\underline{F}}^p = \underline{V}^e \cdot \hat{\underline{F}}^p = Q \cdot \bar{\underline{F}} \tag{1}$$

where $\underline{F}^e = \underline{Q} \cdot \bar{\underline{V}}^e$ is the elastic transformation gradient in which $\bar{\underline{V}}^e$ is the rotated right elastic stretch tensor and $\underline{Q}$ is the rotation tensor which represents the orientation of the rotating frame with respect to the current configuration. The upper bar $(\bar{\cdot})$ for any tensor indicates its rotated form thanks to the orthogonal rotation tensor $\underline{Q}$. While $\bar{\underline{F}}^p$ is the plastic "gradient" with respect to the "isocline" configuration $\bar{C}^p$ and $\bar{\underline{F}}$ is the rotated total transformation gradient as schematized in Fig. 1. The plastic transformation gradient $\hat{\underline{F}}^p = \underline{Q} \cdot \bar{\underline{F}}^p$ corresponds to the transformation obtained by purely elastic unloading from the current configuration C_t.

The fulfillment of the objectivity requirement is based on the rotating frame formulation (see [27,63] and references given there). In this framework, any tensorial quantity (namely $\underline{T}$ for second-rank tensor and $\underline{\underline{T}}$ for fourth-rank tensor) defined in the current configuration is transported to the rotated configurations $\bar{C}^p$ or $\bar{C}$ according to:

$$\begin{cases} \bar{\underline{T}} = \underline{Q}^T \cdot \underline{T} \cdot \underline{Q} \text{ for second-rank tensors} & (a) \\ \bar{\underline{\underline{T}}} = (\underline{Q} \otimes \underline{Q}^T) : \underline{\underline{T}} : (\underline{Q}^T \otimes \underline{Q}) \text{ for fourth-rank tensors} & (b) \end{cases} \tag{2}$$

The use of Eq. (1), together with that of the small elastic strain assumption (i.e. $\bar{\underline{V}}^e = \underline{1} + \bar{\underline{\varepsilon}}^e$ with $\|\bar{\underline{\varepsilon}}^e\| \ll 1$ and $\underline{1}$ being the second-rank unit tensor) in the expression of the spatial velocity gradient ($\bar{\underline{L}} = \dot{\bar{\underline{F}}} \cdot \bar{\underline{F}}^{-1}$), leads to the additive decomposition of the total strain rate as well as the rotating frame rate (or spin) under the following form [63]:

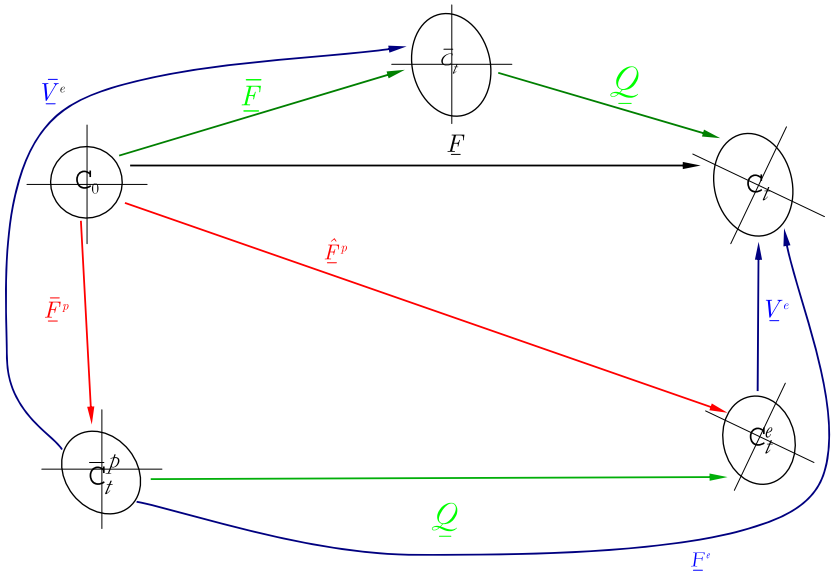

Fig. 1. The kinematics of the elastoplastic transformation in the framework of the rotating frame concept.

$$\begin{cases} \bar{\underline{D}} = [\bar{\underline{L}}]^{\mathrm{S}} = \dot{\bar{\underline{\varepsilon}}}^{\mathrm{e}} + 2[\bar{\underline{\varepsilon}}^{\mathrm{e}} \cdot \bar{\underline{W}}]^{\mathrm{S}} + \bar{\underline{D}}^{\mathrm{p}} = \dot{\bar{\underline{\varepsilon}}}^{\mathrm{eJ}} + \bar{\underline{D}}^{\mathrm{p}} \quad (a) \\ \underline{W}^{\mathrm{Q}} = \dot{\underline{Q}} \cdot \underline{Q}^{\mathrm{T}} = \underline{W} - \bar{\underline{W}} = \underline{W} - [\underline{\underline{K}}(\bar{\underline{V}})] : \bar{\underline{D}} \quad (b) \end{cases} \tag{3}$$

where $\bar{\underline{D}}^{\mathrm{p}} = [\bar{\underline{L}}^{\mathrm{p}}]^{\mathrm{S}} = [\dot{\bar{\underline{F}}}^{\mathrm{p}}.(\bar{\underline{F}}^{\mathrm{p}})^{-1}]^{\mathrm{S}}$ is the plastic strain rate, $\bar{\underline{D}} = [\bar{\underline{L}}]^{\mathrm{S}}$ and $\bar{\underline{W}}$ are the total strain rate and the relative total spin respectively with respect to the Jaumann rotating frame rate, and $\dot{\bar{\underline{\varepsilon}}}^{\mathrm{eJ}}$ defines the rotated Jaumann rate of the small elastic strain tensor.

The total spin is defined as $\underline{W} = [\dot{\underline{F}} \cdot \underline{F}^{-1}]^{A}$. Note that the superscripts $[\cdot]^{\mathrm{S}}$ and $[\cdot]^{\mathrm{A}}$ stand for symmetric and skew-symmetric parts of $[\cdot]$ respectively. The relative total spin $\bar{W}_{ij}$ is postulated a priori as a linear function of the total strain rate: $\bar{\underline{W}} = [\underline{\underline{K}}(\bar{\underline{V}})] : \bar{\underline{D}}$ in which $\underline{\underline{K}}(\bar{\underline{V}})$ is a fourth-rank tensor depending on the rotated total right stretch tensor $\bar{\underline{V}}$. Note that the Jaumann rotating frame is defined by $\underline{\underline{K}} \equiv \underline{0}$ and various other cases can be defined as discussed in [63]. Note that this simple kinematics is quite different from other kinematics that introduce an extended multiplicative decomposition of the transformation gradient of the form $\underline{F} = \underline{F}^{\mathrm{e}} \cdot \underline{F}^{\mathrm{p}} \cdot \underline{F}^{\mathrm{d}}$ where $\underline{F}^{\mathrm{d}}$ is an additional metric associated with the so-called "damage-driven deformation" as described in [75,76].

To simplify the mathematical notations, the upper bar indicating the rotated tensorial variables is deleted below throughout the paper.

2.2. Damage variable, damage-effect tensor and effective state variables

In continuum damage mechanics framework, the ductile damage can be represented either by scalar variables or by tensorial variables of different ranks. For many bulk solids, the use of the isotropic damage theory in which the damage is represented by a scalar variable (d) is sufficient to describe the distribution of the ductile defects. However, for the textured polycrystalline metallic materials as the sheets obtained by rolling, the microcracks develop in preferred directions controlled by the loading directions. In that case, the use of anisotropic damage theory, in which the damage variable is of tensorial nature, is required. For the most metallic materials, it has been shown that a second-rank damage tensor $\underline{d}$ (or d_{ij}) is sufficient to describe the orthotropic distribution of microcracks [77–89,75,76,90,69] (among others).

Let us write the second-rank damage tensor $\underline{d}$ under the following matrix form:

$$\underline{d} = \begin{pmatrix} d_{11} & d_{12} & d_{13} \\ d_{12} & d_{22} & d_{23} \\ d_{13} & d_{23} & d_{33} \end{pmatrix} = \underbrace{\begin{pmatrix} n_1^1 & n_2^1 & n_3^1 \\ n_1^2 & n_2^2 & n_3^2 \\ n_1^3 & n_2^3 & n_3^3 \end{pmatrix}}_{[\underline{R}]} \underbrace{\begin{pmatrix} d_1 & 0 & 0 \\ 0 & d_2 & 0 \\ 0 & 0 & d_3 \end{pmatrix}}_{[\underline{d}^{\Delta}]} \underbrace{\begin{pmatrix} n_1^1 & n_1^2 & n_1^3 \\ n_2^1 & n_2^2 & n_2^3 \\ n_3^1 & n_3^2 & n_3^3 \end{pmatrix}}_{[\underline{R}]^{\mathrm{T}}} \tag{4}$$

where the eigenvalues of the second-rank symmetric damage tensor $0 \leq d_k \leq 1$ ($k \in \{1, 2, 3\}$) represent the orthogonal families of micro-defects and (n_i^k) defines its principal basis. The orthogonal tensor $\underline{P}$ defines the transfer matrix between the working basis and the damage principal basis. The isotropic damage d corresponds to the case where the density of micro-defects is independent of the orientation of each surface. In this isotropic case, the total failure of the RVE (Representative

Volume Element) is achieved when the final fracture condition is reached, i.e. $d = d_c \approx 0.99$. However, the failure condition in the case of anisotropic damage is not trivial and a simple final fracture criterion assumes that the RVE is failed when the highest damage eigenvalue reaches its critical value: $\mathrm{Max}_{k=1..3}(d_k) = d_c = 0.99$.

Once the damage variable defined, the effective state variables can be introduced in the framework of the total energy equivalence assumption and using the so called damage effect tensor of rank four $\underline{\underline{M}}$ (or M_{ijkl}). Different forms of the damage effect tensor have been considered in the literature [78–80,82,86,91–94] (among many others). In this work, the form proposed by [93] is generalized and rewritten here, in the rotated configuration, in the following form (in Eqs. (4)–(6), the indicial notations are used for clarity):

$$\begin{cases} M_{ijkl} = \dfrac{1}{2}(h_{ik}h_{jl} + h_{il}h_{jk}) - \dfrac{1}{3}(h_{ij}^2\delta_{kl} + h_{kl}^2\delta_{ij}) + \dfrac{1}{9}h_{nn}^2\delta_{ij}\delta_{kl} + \dfrac{1}{3}\sqrt{(1 - \|\underline{d}\|_1)^{\eta}}\delta_{ij}\delta_{kl} & (a) \\ \text{where} & \\ h_{ij} = (\delta_{ij} - d_{ij})^{1/k} & (b) \\ \|\underline{d}\|_1 = \dfrac{1}{3}(d_{ij}\delta_{ij}) = \dfrac{1}{3}d_{ii} & (c) \end{cases} \tag{5}$$

This form has the advantage to affect differently the deviatoric and hydrostatic parts of each tensorial state variable, since the damage effect tensor $M_{ijkl} = M^D_{ijkl} + M^H_{ijkl}$ is additively decomposed into a deviatoric $[\cdot]^D$ tensor affecting only the deviatoric part of any tensor and a hydrostatic $[\cdot]^H$ part affecting the hydrostatic part of a tensor:

$$\begin{cases} M^D_{ijkl} = \dfrac{1}{2}(h_{ik}h_{jl} + h_{il}h_{jk}) - \dfrac{1}{3}(h_{ij}^2\delta_{kl} + h_{kl}^2\delta_{ij}) + \dfrac{1}{9}h_{nn}^2\delta_{ij}\delta_{kl} & (a) \\ \text{and} & \\ M^H_{ijkl} = \dfrac{1}{3}\sqrt{(1 - \|\underline{d}\|_1)^{\eta}}\delta_{ij}\delta_{kl} & (b) \end{cases} \tag{6}$$

The parameters η and k are material constants governing the effect of the ductile damage on the hydrostatic and deviatoric stress parts respectively. It is worth noting that M^{D}_{ijkl} defined by Eq. (6a) leads to the one initially proposed by [93] if $k = 2$ in Eq. (5b), while M^{H}_{ijkl} defined by Eq. (6b) is quite different from the one used by Lemaitre and Desmorat [93] which is $\underline{\underline{M}}^H = \frac{1}{3}(1 - \eta\|\underline{d}\|_1)(\underline{1} \otimes \underline{1})$ where $\underline{1}$ is the second-rank unit (Kronecker) tensor. On the other hand, the first term of the RHS of Eq. (6a) defines the damage-effect tensor proposed by [94] if $k = 2$ in Eq. (5b).

Finally let us indicate that, using the classical Voigt notations, the damage-effect operator M_{ijkl} has the following matrix form expressed in the damage eigenvectors basis:

$$M_{ijkl} = \begin{pmatrix} \frac{4}{9}h_1^2 + \frac{1}{9}(h_2^2 + h_3^2) & \frac{1}{9}h_3^2 - \frac{2}{9}(h_1^2 + h_2^2) & \frac{1}{9}h_2^2 - \frac{2}{9}(h_1^2 + h_3^2) & 0 & 0 & 0 \\ & \frac{4}{9}h_2^2 + \frac{1}{9}(h_1^2 + h_3^2) & \frac{1}{9}h_1^2 - \frac{2}{9}(h_2^2 + h_3^2) & 0 & 0 & 0 \\ & & \frac{4}{9}h_3^2 + \frac{1}{9}(h_1^2 + h_2^2) & 0 & 0 & 0 \\ & & & \frac{1}{2}h_1h_2 & 0 & 0 \\ & sym & & & \frac{1}{2}h_2h_3 & 0 \\ & & & & & \frac{1}{2}h_1h_3 \end{pmatrix}$$
$$+ \frac{1}{3}\sqrt{(1 - \|\underline{d}\|_1)^{\eta}} \begin{pmatrix} 1 & 1 & 1 & 0 & 0 & 0 \\ & 1 & 1 & 0 & 0 & 0 \\ & & 1 & 0 & 0 & 0 \\ & & & 0 & 0 & 0 \\ & sym & & & 0 & 0 \\ & & & & & 0 \end{pmatrix} \tag{7}$$

where h_i are the eigenvalues of the effective damage second-rank tensor h_{ij} defined by Eq. (5b). This matrix is symmetric but not diagonal compared to the form discussed in [79].

Let us consider that, in the current deformed and damaged configuration C_t, the mechanical state of the material is described by both external and internal couples of state variables. In the framework of classical local (Cauchy) continuum the two following couples of external state variables are used [95]: $(\underline{\varepsilon} = \int_t \underline{D}\mathrm{d}t, \underline{\sigma})$ the total strain tensor associated with the Cauchy stress tensor, and (T, s) the absolute temperature associated with the specific entropy. Concerning the internal state variables representing the dissipative phenomena, the following couples are used: $(\underline{\varepsilon}^{\mathrm{e}}, \underline{\sigma})$ the small elastic strain tensor and the Cauchy stress tensor, representing the elastoplasticity; $(\underline{\alpha}, \underline{X})$ internal deviatoric strain and stress tensors representing the kinematic hardening; (r, R) the internal strain and stress representing the isotropic hardening; $(\underline{d}, \underline{Y})$ the damage tensor and the associated energy release rate tensor representing the ductile damage; and $(\vec{q}/T, \vec{g} = \overrightarrow{\mathrm{grad}}(T))$ the heat flux vector normalized by the absolute temperature associated with the gradient of the absolute temperature representing the heat exchanges.

According to the total energy equivalence assumption, in the fictive undamaged and rotated configuration $\tilde{C}_t$, the mechanical state is described by the couples of effective state variables $(\underline{\tilde{\varepsilon}}^{\mathrm{e}}, \underline{\tilde{\sigma}})$ or $(\underline{\varepsilon}^{\mathrm{e}}, \underline{\sigma})$, $(\underline{\tilde{\alpha}}, \underline{\tilde{X}})$ and $(\tilde{r}, \tilde{R})$ so that the total energy defined in the tow configurations is the same [27,48,72,79]. This leads to the following definition of the effective state variables:

$$\underline{\tilde{\varepsilon}}^{\mathrm{e}} = \underline{\underline{M}} : \underline{\varepsilon}^{\mathrm{e}} \quad (a) \quad \text{and} \quad (b) \quad \underline{\tilde{\sigma}} = \underline{\underline{M}}^{-1} : \underline{\sigma} \tag{8}$$

$$\underline{\tilde{\alpha}} = \underline{\underline{M}} : \underline{\alpha} \quad (a) \quad \text{and} \quad (b) \quad \underline{\tilde{X}} = \underline{\underline{M}}^{-1} : \underline{X} \tag{9}$$

$$\tilde{r} = \sqrt{1 - \|\underline{d}\|_2^{\gamma}}\, r \quad (a) \quad \text{and} \quad (b) \quad \tilde{R} = \frac{R}{\sqrt{1 - \|\underline{d}\|_2^{\gamma}}} \tag{10}$$

where use has been made of the following notation: $\|\underline{d}\|_2 = \sqrt{\frac{1}{3}\underline{d} : \underline{d}} = \sqrt{\frac{1}{3} d_{ij} d_{ij}}$ to define the norm of the damage tensor and γ is a material parameter governing the effect of the ductile damage on isotropic hardening. Note that, through this choice, the damage affects the elastic behavior and the kinematic hardening through the fourth-rank (symmetric and positive definite) damage-effect tensor $\underline{\underline{M}}$ and the isotropic hardening through the scalar valued function $\sqrt{1 - \|\underline{d}\|_2^{\gamma}}$ [27]. The parameter k in Eq. (5b) is fixed to the value $k = 4$ in order to recover the classical relationships developed in our previous works for the isotropic damage case [27,41,48,63]. Note that, in the fully isotropic damage case, the damage tensor reduces to $\underline{d} = \|\underline{d}\|_1 \cdot \underline{1}$ and $\underline{h} = (1 - \|\underline{d}\|_1)^{1/4} \underline{1}$; while the damage-effect operator reduces to $\underline{\underline{M}} = \sqrt{1 - d}\,\underline{\underline{1}}$ ($\underline{\underline{1}}$ being the fourth-rank unit tensor) with $\eta = 1$ so that the equations Eqs. (8) to (10) become:

$$\begin{cases} \underline{\tilde{\varepsilon}}^{\mathrm{e}} = \sqrt{1 - d}\,\underline{\varepsilon}^{\mathrm{e}} \quad \text{and} \quad \underline{\tilde{\sigma}} = \dfrac{\underline{\sigma}}{\sqrt{1 - d}} & (a) \\ \underline{\tilde{\alpha}} = \sqrt{1 - d}\,\underline{\alpha} \quad \text{and} \quad \underline{\tilde{X}} = \dfrac{\underline{X}}{\sqrt{1 - d}} & (b) \\ \tilde{r} = \sqrt{1 - d^{\gamma}}\, r \quad \text{and} \quad \tilde{R} = \dfrac{R}{\sqrt{1 - d^{\gamma}}} & (c) \end{cases} \tag{11}$$

These effective state variables will be used to derive the state relations as well as the evolution equations from the state and dissipation potentials defined on the fictive undamaged and rotated configuration.

2.3. State potential and state relationships

The state potential has to be defined in the rotated fictive (undamaged) configuration. The global Helmholtz free energy $\rho\psi(\underline{\tilde{\varepsilon}}^{\mathrm{e}}, \underline{\tilde{\alpha}}, \tilde{r}, T)$, positive and convex function of all the effective strain-like state variables in the fictive strain space, is taken as a state potential (ρ is the material density). Note that in this framework of large plastic strains, all the tensorial variables are rotated according to Eq. (2) including the rotated damage tensor $\bar{\underline{d}} = \underline{Q}^{\mathrm{T}} \cdot \underline{d} \cdot \underline{Q}$ which has the same eigenvalues as $\underline{d}$, but rotated with the rotation tensor $\underline{Q}$. For the sake of the notations simplicity, and as mentioned above, the upper bar indicating the rotated tensors will be not used in what follows.

Keeping in mind the symmetry of all the second and fourth-rank tensors, the state potential is written in the rotated fictive configuration as follows:

$$\begin{aligned} \rho\psi\left(\underline{\tilde{\varepsilon}}^{\mathrm{e}}, \underline{\tilde{\alpha}}, \tilde{r}, T\right) &= \frac{1}{2}\underline{\tilde{\varepsilon}}^{\mathrm{e}} : \underline{\underline{\Lambda}} : \underline{\tilde{\varepsilon}}^{\mathrm{e}} - (T - T_r)\underline{P}_t : \underline{\tilde{\varepsilon}}^{\mathrm{e}} - \rho\frac{c_\varepsilon}{2T_r}(T - T_r)^2 + \frac{1}{2}\underline{\tilde{\alpha}} : \underline{\underline{C}} : \underline{\tilde{\alpha}} + \frac{1}{2}Q\tilde{r}^2 \qquad (a) \\ &= \frac{1}{2}\left(\underline{\varepsilon}^{\mathrm{e}} : \underline{\underline{M}}\right) : \underline{\underline{\Lambda}} : \left(\underline{\underline{M}} : \underline{\varepsilon}^{\mathrm{e}}\right) - (T - T_r)\underline{P}_t : \underline{\underline{M}} : \underline{\varepsilon}^{\mathrm{e}} - \rho\frac{c_\varepsilon}{2T_r}(T - T_r)^2 \\ &\quad + \frac{1}{2}C(\underline{\alpha} : \underline{\underline{M}}) : \underline{\underline{C}} : (\underline{\underline{M}} : \underline{\alpha}) + \frac{1}{2}Q\left(1 - \|\underline{d}\|_2^{\gamma}\right)r^2 \qquad (b) \\ &= \frac{1}{2}\underline{\varepsilon}^{\mathrm{e}} : \underline{\tilde{\Lambda}} : \underline{\varepsilon}^{\mathrm{e}} - (T - T_r)\underline{\tilde{P}}_t : \underline{\varepsilon}^{\mathrm{e}} - \rho\frac{c_\varepsilon}{2T_r}(T - T_r)^2 + \frac{1}{2}\underline{\alpha} : \underline{\tilde{\underline{C}}} : \underline{\alpha} + \frac{1}{2}\tilde{Q}r^2 \qquad (c) \end{aligned} \tag{12}$$

where $\underline{\underline{\Lambda}} = 2\mu_{\mathrm{e}}\underline{\underline{1}} + \lambda_{\mathrm{e}}\underline{1} \otimes \underline{1} = 2\mu_{\mathrm{e}}\underline{\underline{1}} + 3\kappa_{\mathrm{e}}\underline{1} \otimes \underline{1}$ is the symmetric fourth-rank tensor defining the material elastic properties of the undamaged isotropic elastic material, where μ_{e} and λ_{e} are the classical Lame's constants and $\kappa_{\mathrm{e}} = (2\mu_{\mathrm{e}} + 3\lambda_{\mathrm{e}})/3$ is the compressibility modulus, $\underline{P}_t$ is the symmetric second-rank thermal expansion tensor which is given by $\underline{P}_t = \alpha_t\underline{1}$ if the thermal expansion is fully isotropic, defined by the single scalar α_t, c_ε is the specific heat and T_{r} is the reference temperature. The fourth-rank (isotropic, symmetric and positive definite) tensor $\underline{\underline{C}} = (2/3)C\underline{\underline{1}}^{\mathrm{dev}}$ and the scalar Q are the kinematic and the isotropic hardening modules, respectively, while α_{t} is the thermal dilatation parameter. Note that all these material parameters are temperature dependent. Their damage-affected values used in Eq. (12c) are given throughout Eqs. (6), (7) and (8) by:

$$\underline{\underline{\tilde{\Lambda}}} = \underline{\underline{M}}^{\mathrm{T}} : \underline{\underline{\Lambda}} : \underline{\underline{M}} = \underline{\underline{M}}^{\mathrm{T}} : [2\mu_{\mathrm{e}}\underline{\underline{1}} + \lambda_e \underline{1} \otimes \underline{1}] : \underline{\underline{M}} = 2\mu_{\mathrm{e}}\underline{\underline{M}}^{\mathrm{T}} : \underline{\underline{M}} + \lambda_{\mathrm{e}}\left(\underline{\underline{M}}^{\mathrm{T}} : \underline{1}\right) \otimes (\underline{1} : \underline{\underline{M}}) \tag{13}$$

$$\underline{\underline{\tilde{C}}} = \underline{\underline{M}}^{\mathrm{T}} : \underline{\underline{C}} : \underline{\underline{M}} = \frac{2}{3} C \underline{\underline{M}}^{\mathrm{T}} : \underline{\underline{M}} \tag{14}$$

$$\tilde{Q} = Q\left(1 - \|\underline{d}\|_2^{\gamma}\right) \tag{15}$$

$$\underline{\tilde{P}}_t = \underline{P}_t : \underline{\underline{M}} = \alpha_t \underline{1} : \underline{\underline{M}} = \alpha_t \underline{\underline{M}} : \underline{1} \tag{16}$$

Clearly, the tensors $\underline{\underline{\tilde{\Lambda}}}$, $\underline{\underline{\tilde{C}}}$ and $\underline{\tilde{P}}_t$ lose their initial isotropy due to the damage-induced anisotropy throughout the damage-effect tensor $\underline{\underline{M}}$.

The stress-like variables, which are the state relations, are easily derived from the state potential (Eq. (12c)):

$$\underline{\sigma} = \rho \frac{\partial \psi}{\partial \underline{\varepsilon}^{\mathrm{e}}} = \underline{\underline{\tilde{\Lambda}}} : \underline{\varepsilon}^{\mathrm{e}} - (T - T_r)\underline{\tilde{P}}_t \tag{17}$$

$$\underline{X} = \rho \frac{\partial \psi}{\partial \underline{\alpha}} = \underline{\underline{\tilde{C}}} : \underline{\alpha} \tag{18}$$

$$R = \rho \frac{\partial \psi}{\partial r} = \tilde{Q} r \tag{19}$$

$$s = -\frac{\partial \psi}{\partial T} = \frac{1}{\rho}\underline{\tilde{P}}_t : \underline{\varepsilon}^{\mathrm{e}} + \frac{c_\varepsilon}{T_r}(T - T_r) \tag{20}$$

$$\begin{cases} \underline{Y} = -\rho \dfrac{\partial \psi}{\partial \underline{d}} = \underline{Y}^{\mathrm{e}} + \underline{Y}^{\alpha} + \underline{Y}^{r} & (a) \\ \text{where} & \\ \underline{Y}^{\mathrm{e}} = -\dfrac{1}{2}\underline{\varepsilon}^{\mathrm{e}} : \left[\dfrac{\partial \underline{\underline{\tilde{\Lambda}}}}{\partial \underline{d}}\right] : \underline{\varepsilon}^{\mathrm{e}} + (T - T_r)\left[\dfrac{\partial \underline{\tilde{P}}_t}{\partial \underline{d}}\right] : \underline{\varepsilon}^{\mathrm{e}} & (b) \\ \underline{Y}^{\alpha} = -\dfrac{1}{2}\underline{\alpha} : \left[\dfrac{\partial \underline{\underline{\tilde{C}}}}{\partial \underline{d}}\right] : \underline{\alpha} & (c) \\ \underline{Y}^{r} = +\dfrac{\gamma}{6} Q r^2 \|\underline{d}\|_2^{\gamma-2} \underline{d} & (d) \end{cases} \tag{21}$$

Note that the damage energy density release rate (Eq. (21)), symmetric second-rank tensor, is additively decomposed into three contributions coming from elasticity $\underline{Y}^{\mathrm{e}}$, kinematic hardening $\underline{Y}^{\alpha}$, and isotropic hardening $\underline{Y}^{r}$ [27,72].

Using Eqs. (13) to (16) with the help of Eq. (6) the above state relations can be expressed under the following indicial form:

$$\sigma_{ij} = 2\mu_e \left(h^2_{im}\varepsilon^{\mathrm{eD}}_{ml}h^2_{lj}\right)^D + \kappa_e\left(1 - \frac{1}{3}d_{nn}\right)^{\eta}\varepsilon^{\mathrm{e}}_{rr}\delta_{ij} - \alpha_t(T - T_r)\sqrt{\left(1 - \frac{1}{3}d_{nn}\right)^{\eta}}\delta_{ij} \tag{22}$$

$$X_{ij} = \frac{2}{3}C\left(h^2_{im}\alpha_{ml}h^2_{lj}\right)^D \tag{23}$$

$$R = Q\left(1 - \|\underline{d}\|_2^{\gamma}\right)r \tag{24}$$

$$s = \frac{\alpha_t}{\rho}\sqrt{\left(1 - \frac{1}{3}d_{nn}\right)^{\eta}}\varepsilon^{\mathrm{e}}_{kk} + \frac{c_\varepsilon}{T_r}(T - T_r) \tag{25}$$

$$Y^{\mathrm{e}}_{ij} = -2\mu_e\varepsilon^{\mathrm{eD}}_{rk}h^2_{km}\varepsilon^{\mathrm{eD}}_{ml}\frac{\partial h^2_{lr}}{\partial d_{ij}} + \frac{\kappa_e\eta}{6}\left(1 - \frac{1}{3}d_{nn}\right)^{\eta-1}\left(\varepsilon^{\mathrm{e}}_{rr}\right)^2\delta_{ij} + \frac{\alpha_t\eta}{6}(T - T_r)\left(1 - \frac{1}{3}d_{nn}\right)^{(\eta-2)/2}\left(\varepsilon^{\mathrm{e}}_{rr}\right)\delta_{ij} \tag{26}$$

$$Y^{\alpha}_{ij} = -\frac{2}{3}C\alpha_{rk}h^2_{km}\alpha_{ml}\frac{\partial h^2_{lr}}{\partial d_{ij}} \tag{27}$$

$$Y^{r}_{ij} = \frac{\gamma}{6}Qr^2\left(\sqrt{\frac{1}{3}d_{kl}d_{kl}}\right)^{\gamma-2}d_{ij} \tag{28}$$

The derivatives of the effective damage-effect function h^2_{ij} appearing in Eq. (26) and Eq. (27) are developed in detail in [69].

The close examination of the elastic contribution Y^{e}_{ij} given by Eq. (26) shows that the latter contains separately the effect of the deviatoric strain (the first term of the RHS of Eq. (26)), which is expected to govern the shear damage growth, while the second term of the RHS of Eq. (26) is spherical in nature and controls the isotropic growth of voids under hydrostatic stress state. The kinematic hardening contribution defined by Eq. (27) governs exclusively the shear damage due to the

deviatoric nature of the back strain tensor $\underline{\alpha}$. The isotropic hardening contribution Y_{ij}^{r} (Eq. (28)) is directly dependent on the damage directions, giving an anisotropic damage evolution despite the isotropic character of the hardening.

Finally, let us note that, if the damage is isotropic, $d_{ij} = d\delta_{ij}$ and $\eta = 1$, leading to $M_{ijkl} = \sqrt{1-d}\delta_{ik}\delta_{jl}$, the damage energy density release rate reduces to its classical form, developed in our previous works [27,48,63,72].

In metal forming, even if the tool kinematics is monotonic, some material points can be found in compression after tension or vice versa, depending on the forming tool geometry. On the other hand, it is well known that when an RVE is subjected to tension loading until some microcracks are created, then the applied loading direction is inverted in compression, the created microcracks tend to close, giving a clear decrease in the damage growth under compression. The usual way to describe this effect is to decompose the tensorial state variables into positive and negative parts and to affect them differently by the damage variable [83,84,86,88,96,93,97–105] (among many others). This gives satisfaction as long as the damage is isotropic; however, in the presence of anisotropic damage, many difficulties arise related to a loss of continuity and/or convexity of the state and dissipation potentials [83,84,99,103,105].

The simplest way to describe this microcrack closure effect without introducing the loss of convexity and continuity of the state and/or dissipation potentials is to apply the spectral decomposition of the state variables, which contribute to the definition of the damage energy density release rate $\underline{Y}$ as defined by Eqs. (26)–(29) [69]. The decomposition into positive and negative parts of any symmetric second-rank tensor $\underline{T}$ is performed through a spectral decomposition by $\underline{T}^{+} = \sum_{k=1}^{r\leq n} \langle T_k \rangle \underline{E}^{k}$ in which $\langle T_k \rangle$ stands for the positive part of T_k, and $\underline{T}^{-} = \underline{T} - \underline{T}^{+}$ with T_k are the r distinct eigenvalues of the tensor $\underline{T}$ and $\underline{E}^{k} = \vec{e}^{k} \otimes \vec{e}^{k}$ are the eigenprojection tensors in which $\vec{e}^{k}$ are the eigenvectors associated with the eigenvalues T_k. When applied to the two strain-like tensorial state variables $\underline{\tilde{\varepsilon}}^{e}$ and $\underline{\tilde{\alpha}}$ appearing in Eqs. (26) and (27), their associated effective state variables given by Eqs. (8a) and (9a) take the following form:

$$\tilde{\varepsilon}_{ij}^{e} = M_{ijkl+}^{D}\varepsilon_{kl+}^{eD} + \frac{1}{3}\sqrt{\left(1-\|\underline{d}\|_1\right)^{\eta}}\langle\varepsilon_{nn}^{e}\rangle\delta_{ij} + M_{ijkl-}^{D}\varepsilon_{kl-}^{eD} - \frac{1}{3}\sqrt{\left(1-\hbar\|\underline{d}\|_1\right)^{\eta}}\langle-\varepsilon_{nn}^{e}\rangle\delta_{ij} \tag{29}$$

$$\tilde{\alpha}_{ij} = M_{ijkl+}^{D}\alpha_{kl+} + M_{ijkl-}^{D}\alpha_{kl-} \tag{30}$$

with ε_{ij+}^{eD} and ε_{ij-}^{eD} are the positive and negative parts of the deviatoric elastic strain tensor classically defined by $\varepsilon_{ij}^{eD} = \varepsilon_{ij}^{e} - \frac{1}{3}\varepsilon_{kk}^{e}\delta_{ij} = \varepsilon_{ij+}^{eD} + \varepsilon_{ij-}^{eD}$. The damage-effect operator noted M_{ijkl+}^{D} is applied to the positive part of the deviatoric strain and the back strain tensors as defined by Eqs. (6a) and (6b). However, the damage-effect tensor noted M_{ijkl-}^{D} is applied to the negative parts of these deviatoric strain tensors through Eq. (6a) with the effective damage operator $h_{ij-} = (\delta_{ij} - \hbar d_{ij})^{1/4}$ instead of $h_{ij} = (\delta_{ij} - d_{ij})^{1/4}$. The parameter $\hbar (0 \leq \hbar \leq 1)$ represents the microcracks closure effect by reducing the damage effect during the negative parts of the loading path. For metallic materials, the value of this parameter is usually taken as $\hbar = 0.2$ [73], leading to a lower damage growth under compressive loading paths, with two limit cases: (i) $\hbar = 1$, which makes no difference between the damage growth under positive and negative loading paths (no microcracks closure effect), and (ii) $\hbar = 0$, for which damage growth takes place only under the positive loads while no micro defects growth under the compressive phase of the loading paths (full microcrack closure effect).

When these two effective strain-like variables (Eqs. (29) and (30)) are used in the state potential (Eq. (12a)) from which the damage energy density release rate is recalculated, than the following new expressions of the elastic part called $Y_{ij}^{e^*}$ and kinematic hardening part called $Y_{ij}^{\alpha^*}$ are obtained [69]:

$$\begin{aligned} Y_{ij}^{e^*} &= Y_{ij}^{e^*+} + Y_{ij}^{e^*-} \\ &= -2\mu_e\varepsilon_{rk+}^{eD}h_{km}^{2}\varepsilon_{ml+}^{eD}\frac{\partial h_{lr}^{2}}{\partial d_{ij}} + \left[\frac{k_e\eta}{6}\left(1-\frac{1}{3}d_{nn}\right)^{\eta-1}\langle\varepsilon_{rr}^{e}\rangle + \frac{\alpha_t\eta}{6}(T-T_r)\left(1-\frac{1}{3}d_{nn}\right)^{(\eta-2)/2}\right]\langle\varepsilon_{rr}^{e}\rangle\delta_{ij} \qquad (a) \\ &\quad - 2\mu_e\varepsilon_{rk-}^{eD}h_{km-}^{2}\varepsilon_{ml-}^{eD}\frac{\partial h_{lr-}^{2}}{\partial d_{ij}} + \hbar\left[\frac{k_e\eta}{6}\left(1-\frac{\hbar}{3}d_{nn}\right)^{\eta-1}\langle-\varepsilon_{rr}^{e}\rangle + \frac{\alpha_t\eta}{6}(T-T_r)\left(1-\frac{\hbar}{3}d_{nn}\right)^{(\eta-2)/2}\right]\langle-\varepsilon_{rr}^{e}\rangle\delta_{ij} \qquad (b) \end{aligned} \tag{31}$$

$$Y_{ij}^{\alpha^*} = Y_{ij}^{\alpha^*+} + Y_{ij}^{\alpha^*-} = -\frac{2}{3}C\alpha_{rk+}h_{km}^{2}\alpha_{ml+}\frac{\partial h_{lr}^{2}}{\partial d_{ij}} - \frac{2}{3}C\alpha_{rk-}h_{km-}^{2}\alpha_{ml-}\frac{\partial h_{lr-}^{2}}{\partial d_{ij}} \tag{32}$$

where $\bar{Y}_{ij}^{e^*+}$ and $\bar{Y}_{ij}^{e^*-}$ (respectively $\bar{Y}_{ij}^{\alpha^*+}$ and $\bar{Y}_{ij}^{\alpha^*-}$) are the elastic (respectively kinematic hardening) contributions depending respectively on the positive and negative parts of the elastic strain tensor (respectively kinematic hardening strain tensor).

The following particular cases can be obtained from Eqs. (31) and (32):

- for anisotropic damage:
  - without microcracks closure ($\hbar = 1$): the damage evolves identically under positive or negative loading paths according to Eqs. (26) and (27),
  - with full microcracks closure effect ($\hbar = 0$): the damage evolves only under the positive phase of the loading path governed by the following damage energy density release rate related to elasticity and kinematic hardening:

$$\begin{cases} Y_{ij}^{e^*} = Y_{ij}^{e+*} = -2\mu_e \varepsilon_{rk+}^{eD} h_{km}^2 \varepsilon_{ml+}^{eD} \dfrac{\partial h_{lr}^2}{\partial d_{ij}} + \dfrac{k_e \eta}{6}(1-\dfrac{1}{3}d_{nn})^{\eta-1}\langle\varepsilon_{rr}^e\rangle^2\delta_{ij} + \dfrac{\alpha_t \eta}{6}(T-T_r)(1-\dfrac{1}{3}d_{nn})^{(\eta-2)/2}\langle\varepsilon_{rr}^e\rangle\delta_{ij} & (a) \\ Y_{ij}^{\alpha^*} = Y_{ij}^{\alpha+*} = \dfrac{2}{3} C\alpha_{rk+} h_{km}^2 \alpha_{ml+} \dfrac{\partial h_{lr}^2}{\partial d_{ij}} & (b) \end{cases} \tag{33}$$

- for isotropic damage:
  - without microcracks closure ($\hbar = 1$), the damage evolves identically in tension and in compression, driven by:

$$\begin{cases} Y_{ij}^{e^*} = Y_{ij}^{e} = \dfrac{1}{3}\left[\mu_e \varepsilon_{kl}^{eD}\varepsilon_{kl}^{eD} + \dfrac{k_e\eta}{6}(1-d)^{\eta-1}\varepsilon_{rr}^e + \dfrac{\alpha_t\eta}{6}(T-T_r)(1-d)^{(\eta-2)/2}\right]\varepsilon_{rr}^e\delta_{ij} & (a) \\ Y_{ij}^{\alpha^*} = Y_{ij}^{\alpha} = \dfrac{1}{3}\left[\dfrac{1}{3}C\alpha_{kl}\alpha_{kl}\right]\delta_{ij} & (b) \end{cases} \tag{34}$$

  - with full microcracks closure effect ($\hbar = 0$): the damage evolves only in tension, driven by the positive parts of the damage energy density release rate, given by:

$$\begin{cases} Y_{ij}^{e^*} = Y_{ij}^{e+*} = \dfrac{1}{3}\left[\mu_e \varepsilon_{kl+}^{eD}\varepsilon_{kl+}^{eD} + \dfrac{k_e\eta}{6}(1-d)^{\eta-1}\langle\varepsilon_{rr}^e\rangle + \dfrac{\alpha_t\eta}{6}(T-T_r)(1-d)^{(\eta-2)/2}\right]\langle\varepsilon_{rr}^e\rangle\delta_{ij} & (a) \\ Y_{ij}^{\alpha^*} = Y_{ij}^{\alpha+*} = \dfrac{1}{3}\left[\dfrac{1}{3}C\alpha_{kl+}\alpha_{kl+}\right]\delta_{ij} & (b) \end{cases} \tag{35}$$

    while under the negative hydrostatic strain $\langle -\varepsilon_{rr}^e\rangle$ the damage cannot evolve, since $\hbar = 0$ in Eq. (31b).

2.4. Yield function, dissipation potential and evolution relationships

After the derivation of the state relations from an appropriate state potential as discussed in §2.3 above, the derivation of the evolution equations relative to the dissipative phenomena have to be performed based on the following Clausius–Duhem inequality expressing the positivity of the volumic dissipation $\wp_V$ (see for example [27]):

$$\begin{cases} \wp_V = \wp_{Int} + \wp_{Th} \geq 0 & (a) \\ \text{with} & \\ \wp_{Int} = \underline{\sigma} : \underline{D}^p - \underline{X} : \dot{\underline{\alpha}} - R\dot{r} + \underline{Y} : \dot{\underline{d}} \geq 0 & (b) \\ \wp_{Th} = -\dfrac{\vec{q}}{T} \cdot \overrightarrow{\text{grad}}(T) \geq 0 & (c) \end{cases} \tag{36}$$

Since the stress-like variables $\{\underline{\sigma}, \underline{X}, R, \underline{Y}\}$ are known from the state potential (see §2.3) and $\overrightarrow{\text{grad}}(T)$ is known as soon as the temperature is known, the fluxes variables $\{\underline{D}^p, \dot{\underline{\alpha}}, \dot{r}, \dot{\underline{d}}, \vec{q}/T\}$ should be determined from appropriate dissipation potentials in such a manner that the dissipation inequalities Eq. (36a), and consequently Eqs. (36b) and (36c) are identically fulfilled.

Let us first examine the thermal dissipation defined by Eq. (36c) in order to extract the generalized heat equation (the reader is referred to [27] for the details of the formulation). The heat flux vector is easily derived from the classical Fourier potential as a convex function of the associated stress-like variable $\vec{g} = \overrightarrow{\text{grad}}(T)$. Assuming the isotropy of the thermal conductivity represented by the unimodular (spherical) symmetric second-rank tensor $\underline{k} = k\underline{1}$, in which k is temperature-dependent thermal conductivity of the material, the Fourier potential given by:

$$\varphi_{th}^*(\vec{g}; T) = \frac{1}{2}\vec{g}\cdot\underline{k}\cdot\vec{g} = \frac{k}{2}\vec{g}\cdot\vec{g} \tag{37}$$

allows the derivation of the heat flux vector by:

$$\frac{\vec{q}}{T} = -\frac{\partial\varphi_{th}^*(\vec{g}; T)}{\partial\vec{g}} = -\underline{k}\cdot\vec{g} = -k\vec{g} \tag{38}$$

If, as usually observed, k is inversely proportional to the temperature T, than the classical Fourier linear relationship $\vec{q} = -k_0\vec{g}$ (where is the temperature-independent thermal conductivity) is recovered from Eq. (38).

Now with the help of Eq. (38) and using the first law of thermodynamics expressing energy conservation, the following partial differential equation or heat equation is easily obtained [27] under the following general form:

$$-\text{div}(\vec{q}) - \rho T\frac{\partial s}{\partial T}\dot{T} + \wp_{Int} + T\left(\frac{\partial\underline{\sigma}}{\partial T} : \dot{\underline{\varepsilon}}^{eJ} + \frac{\partial\underline{X}}{\partial T} : \dot{\underline{\alpha}} + \frac{\partial R}{\partial T}\dot{r} - \frac{\partial\underline{Y}}{\partial T} : \dot{\underline{d}}\right) = 0 \tag{39}$$

in which $\wp_{\text{Int}}$ is the intrinsic dissipation defined by Eq. (37b). This partial differential equation describes the temperature distribution inside a thermo-elasto-plastic solid containing anisotropic ductile damage, to which appropriate thermal boundary conditions should be added.

Now the intrinsic dissipation is analyzed in the generalized standard material framework [95] assuming the non-associative plasticity theory. If the time-independent plasticity theory is assumed, it is possible to use two independent (but fully coupled) yield functions and two dissipation potentials relative to the plasticity ($f^{\text{p}}, \mathsf{F}^{\text{p}}$) and to the damage ($f^{d}, \mathsf{F}^{d}$) [27,39,48,89]. A detailed analysis of this multiple surfaces non-associative theory can be found in [27]. In this paper, a single surface model is used to describe the fully anisotropic and strongly coupled damaged elastoplastic behavior, using a single yield function $f(\tilde{\underline{\sigma}}, \tilde{\underline{X}}, \tilde{R}; T)$ and plastic potential $\mathsf{F}\ (\tilde{\underline{\sigma}}, \tilde{\underline{X}}, \tilde{R}, \tilde{\underline{Y}}; T)$, both scalar valued, positive and convex functions of their main arguments in the stress space with the temperature acting as the simple parameter, defined here in the rotated fictive configuration:

$$f(\tilde{\underline{\sigma}}, \tilde{\underline{X}}, \tilde{R}; T) = \|\tilde{\underline{\sigma}} - \tilde{\underline{X}}\|_{\text{c}} - \tilde{R} - \sigma_y \leq 0 \tag{40}$$

$$\begin{cases} F(\tilde{\underline{\sigma}}, \tilde{\underline{X}}, \tilde{R}, \underline{Y}; \underline{d}, T) = F^{\text{p}}(\tilde{\underline{\sigma}}, \tilde{\underline{X}}, \tilde{R}; T) + F^{\text{d}}(\underline{Y}; \underline{d}, T) & (a) \\ \text{with} \\ F^{\text{p}}(\tilde{\underline{\sigma}}, \tilde{\underline{X}}, \tilde{R}; T) = \|\tilde{\underline{\sigma}} - \tilde{\underline{X}}\|_{\text{p}} + \dfrac{3a}{4C}\tilde{\underline{X}} : \tilde{\underline{X}} + \tilde{R}\left(\dfrac{b}{2Q}\tilde{R} - 1\right) & (b) \\ F^{\text{d}}(\underline{Y}; \underline{d}, T) = \dfrac{S}{(s+1)(1 - \|\underline{d}\|_1)^{\beta}}\left\langle \dfrac{\|\underline{Y}\|_3 - Y_0}{S} \right\rangle^{s+1} & (c) \end{cases} \tag{41}$$

where σ_y is the initial yield stress, a and b characterize the nonlinearity of the kinematic and the isotropic hardening, respectively. Similarly, the material parameters (β, S, s, Y_0) characterize the nonlinear ductile damage evolution. All these material parameters are temperature dependent. The stress norms $\|\cdot\|_c$ in Eq. (40) and $\|\cdot\|_p$ in Eq. (41b) are the equivalent stresses characterizing the yield criterion and the plastic potential respectively. In this work, the well-known anisotropic Hill48 quadratic equivalent stress is adopted for both:

$$\begin{aligned} \left\|\tilde{\underline{\sigma}}^{D} - \tilde{\underline{X}}\right\|_i &= \sqrt{\left(\tilde{\underline{\sigma}}^{D} - \tilde{\underline{X}}\right) : \underline{\underline{H}}^{i} : \left(\tilde{\underline{\sigma}}^{D} - \tilde{\underline{X}}\right)} \\ &= \sqrt{\left(\underline{\sigma}^{D} - \underline{X}\right) : \tilde{\underline{\underline{H}}}^{i} : \left(\underline{\sigma}^{D} - \underline{X}\right)} \quad \text{with } i \in \{c, p\} \end{aligned} \tag{42}$$

where $\underline{\underline{H}}^{c}$ and $\underline{\underline{H}}^{\text{p}}$ are the initial anisotropic operators of the undamaged material. Each one of these two operators is characterized by six material constants ($F^i, G^i, H^i, L^i, M^i, N^i$) to describe the initial orthotropic plasticity.

The operators $\tilde{\underline{\underline{H}}}^{\text{c}} = (\underline{\underline{M}}^{\text{D}})^{-\text{T}} : \underline{\underline{H}}^{\text{c}} : (\underline{\underline{M}}^{\text{D}})^{-1}$ and $\tilde{\underline{\underline{H}}}^{\text{p}} = (\underline{\underline{M}}^{\text{D}})^{-\text{T}} : \underline{\underline{H}}^{\text{p}} : (\underline{\underline{M}}^{\text{D}})^{-1}$ are the actual anisotropic operators of the damaged RVE, indicating that the plastic anisotropies evolve with the anisotropic damage growth. The deviatoric character of the plastic strain rate tensor is guaranteed by the use of $\underline{\underline{M}}^{\text{D}}$ instead of $\underline{\underline{M}}$. If not, a damage induced volume variation can be taken into account due to the use of the operator $\underline{\underline{M}}$ instead of $\underline{\underline{M}}^{D}$.

In Eq. (41c), the notation $\langle x \rangle$ indicates the positive value of x i.e. $\langle x \rangle = x$ if $x > 0$ and $\langle x \rangle = 0$ if $x \leq 0$ and the norm $\|\underline{Y}\|_3$ is defined by: $\|\underline{Y}\|_3 = \sqrt{3\underline{Y} : \underline{Y}}$.

The following remarks are highlighted:

- the classical associative theory is recovered when taking $\underline{\underline{H}}^{c} = \underline{\underline{H}}^{\text{p}}$,
- the classical isotropic von Mises equivalent stresses are recovered when taking $\underline{\underline{H}}^{\text{c}} = \underline{\underline{H}}^{\text{p}} = \underline{1} \otimes \underline{1} - \frac{1}{3}\underline{\underline{1}}$.

In the framework of this non-associative formulation, the application of the generalized normality rule to the plastic potential F instead of the yield function f, the following evolution equations governing the overall dissipative phenomena:

$$\underline{D}^{\text{p}} = \dot{\lambda}\frac{\partial F}{\partial \underline{\sigma}} = \dot{\lambda} n^{\text{p}} = \dot{\lambda}\left[\underline{\underline{M}}^{\text{D}}\right]^{-1} : \tilde{\underline{n}}^{\text{p}} \quad \text{with} \quad \tilde{\underline{n}}^{\text{p}} = \frac{\underline{\underline{H}}^{\text{p}} : (\tilde{\underline{\sigma}}^{\text{D}} - \tilde{\underline{X}})}{\|\tilde{\underline{\sigma}}^{\text{D}} - \tilde{\underline{X}}\|_{\text{p}}} \tag{43}$$

$$\dot{\underline{\alpha}} = -\dot{\lambda}\frac{\partial F}{\partial \underline{X}} = \underline{D}^{\text{p}} - \dot{\lambda} a \underline{\alpha} \tag{44}$$

$$\dot{r} = -\dot{\lambda}\frac{\partial F}{\partial R} = \dot{\lambda}\left(\frac{1}{\sqrt{1 - \|\underline{d}\|_2^{\gamma}}} - br\right) \tag{45}$$

$$\dot{\underline{d}} = \dot{\lambda}\frac{\partial \mathsf{F}}{\partial \underline{Y}} = \frac{\dot{\lambda}}{(1 - \|\underline{d}\|_1)^{\beta}}\left\langle \frac{\|\underline{Y}\|_3 - Y_0}{S} \right\rangle^{S} \frac{3\underline{Y}}{\|\underline{Y}\|_3} \tag{46}$$

In Eq. (43), $\underline{n}^{p} = \partial F/\partial \underline{\sigma}$ is the outward normal to the plastic potential F in the stress space, while $\underline{\tilde{n}}^{p} = \partial F/\partial \underline{\tilde{\sigma}}$ is the outward normal to F in the effective stress space and $\dot{\lambda}$ is the Lagrange multiplier. For this case of time-independent plasticity, the plastic multiplier $\dot{\lambda} = \dot{\lambda}_p$ is deduced from the classical consistency condition applied to the yield function i.e. $\dot{f} = 0$ if $f = 0$. Its analytical form can be found in [69]; however, when using the FE method, $\dot{\lambda}$ is calculated numerically at each Gauss quadrature point of each finite element during the structure calculation by the FEM.

For time-dependent plasticity or viscoplasticity, it has been shown (see [27,72]) that the same constitutive equations; i.e. the state relationships defined by Eqs. (22) to (35) and the evolution equations (Eqs. (43) to (46) are obtained. The sole difference comes from the expression of the Lagrange multiplier, which is now denoted $\dot{\lambda} = \dot{\lambda}_{vp}$ and given by:

$$\dot{\lambda}_{vp} = \begin{cases} \langle \frac{f(\tilde{\sigma},\tilde{X},\tilde{R};T)}{K_v} \rangle^{n_v} & \text{Noton–Hoff type} \quad (a) \\ \text{or} & \\ K_{1v} \sinh(\langle \frac{f(\tilde{\sigma},\tilde{X},\tilde{R};T)}{K_{2v}} \rangle) & \text{hyperbolic sine type} \quad (b) \end{cases} \tag{47}$$

in which $f(\tilde{\underline{\sigma}}, \tilde{\underline{X}}, \tilde{R}; T)$ is the yield function defined by Eq. (40); (K_v, n_v) are viscous parameters for Norton–Hoff-type viscoplasticity, while (K_{1v}, K_{2v}) are viscous parameters for hyperbolic-sine type viscoplasticity.

Finally, let's note that the friction between the deformed solid and the tools is based on the well-known Coulomb model implemented in standard way on the ABAQUS explicit base on the master/slave surface techniques.

3. About the numerical resolution schemes

The numerical simulation of metal forming processes consists in solving a highly nonlinear initial and boundary value problem (IBVP) containing two strong forms defined, on the space domain Ω_t and on the time domain $I_t = [t_0\ t_f]$, where t_0 and t_f are the initial and final time, by [27]:

- the equilibrium equations deduced from the principle of the virtual powers ($\vec{f}$ is the body forces vector, $\vec{\gamma}$ is the acceleration vector, $\vec{\vec{F}}$ is the imposed forces on the specified solid boundary oriented by the normal $\vec{n}$ and $\vec{\vec{u}}$ is the imposed displacement on the specified solid boundary):

$$\begin{cases} \overrightarrow{\text{div}}(\underline{\sigma}) + \vec{f} - \rho\vec{\gamma} = 0 & \text{in } \Omega_t, t \in I_t \quad (a) \\ \underline{\sigma} \cdot \vec{n} = \vec{\vec{F}} & \text{on } \Gamma_F \text{ (Neumann)} \quad (b) \\ \vec{u} = \vec{\vec{u}} & \text{on } \Gamma_u \text{ (Dirichlet)} \quad (c) \end{cases} \tag{48}$$

- the heat equations deduced from the first principle of thermodynamics by Eqs. (39) and (38):

$$\begin{cases} k_0 \text{Lap}(T) - \rho T \dfrac{\partial s}{\partial T}\dot{T} + \wp_{\text{Int}} + T\left(\dfrac{\partial \underline{\sigma}}{\partial T} : \dot{\underline{\varepsilon}}^{ej} + \dfrac{\partial \underline{X}}{\partial T} : \dot{\underline{\alpha}} + \dfrac{\partial R}{\partial T}\dot{r} - \dfrac{\partial \underline{Y}}{\partial T} : \dot{\underline{d}}\right) = 0 \quad \text{on } \Omega_t,\ t \in I_t \\ \text{with appropriate Dirichlet and Neumann thermal boundary conditions} \end{cases} \tag{49}$$

in which Lap(T) stands for the Laplacian of the absolute temperature. The weak forms associated with Eqs. (48) and (49) can be easily obtained based on the weighted residual and Galerkin methods. When Ω_t is discretized by the FEM (finite element method) with a variable space size h_x and I_t is discretized by the FDM (finite difference method) with a variable time step size Δt, these two weak forms lead to two nonlinear algebraic systems to be solved on each time increment of the form $[t_n\ t_{n+1} = t_n + \Delta t]$.

Various dynamic implicit or explicit resolution schemes can be adopted to solve these two nonlinear algebraic systems in order to obtain the displacement vector $\vec{u}$ and the temperature T at each node of the structure (see the following general books [106–110] among many other). For metal forming problems where the inelastic strains are very large, the contact with friction is varying and concerns a great number of nodes located and the external boundaries of the deformed solid and due to the damage effect (fully damaged elements deletion), the dynamic explicit scheme is preferred. Here the dynamic explicit resolution scheme is used.

Whatever the global resolution scheme, the state variables ($\underline{\sigma}$ or $(\underline{\varepsilon}^{p})$, $\underline{X}$ or $(\underline{\alpha}^{p})$, R or (r), $\underline{Y}$ or $(\underline{d})$ and $\vec{q}$) have to be calculated at each Gauss point of each element in order to compute the internal force vector. This is performed using the iterative fully implicit integration scheme based on the elastic prediction and inelastic correction algorithm applied to the reduced number of equations, i.e. only two scalar equations with two unknowns namely $\Delta\lambda$ (i.e. $\Delta\lambda_p$ or $\Delta\lambda_{vp}$) and d_{n+1} for the fully isotropic case, or three equations (with two of tensorial nature) with three unknowns namely $\Delta\lambda$ (i.e. $\Delta\lambda_p$ or $\Delta\lambda_{vp}$), $\underline{n}^{p}_{n+1}$ and $\underline{d}_{n+1}$ in the case of fully anisotropic flow (i.e. anisotropy of large inelastic strains and ductile damage).

Various versions of these models as well as some specific elements have been developed and implemented in ABAQUS/Explicit through the user's subroutines VUMAT (to implement the fully coupled advanced constitutive equations) and VUEL (to implement the specific elements). This implementation was made in such a manner that the computation can

Table 1
Elastoplastic parameters for the overall three models.

E (GPa)	ν (–)	σ_y (MPa)	C (GPa)	a	Q (GPa)	b (–)	F_C (–)
195.0	0.3	300	7.0	170.0	2.6	1.5	0.863

G_C (–)	H_C (–)	$N_C = L_C = M_C$ (–)	F_p (–)	G_p (–)	H_p (–)	$N_p = L_p = M_p$ (–)
0.800	0.200	1.452	0.461	0.447	0.553	1.400

Table 2
Damage parameters for each of the three models.

	S (J/mm^3)	s	β	Y_0 (J/mm^3)	γ	η	$\hbar$	h_x (mm)
Model 1	12	1	1	0	6	1	1	0.5
Model 2	18	1	2	0	6	1	1	0.5
Model 3	18	1	2	0	6	1	0	0.5

be performed with or without damage coupling. The fully damaged elements with the lowest size are deleted in order to reproduce the macroscopic cracks initiation and propagation leading to the creation of new boundaries with adaptive new remeshing methodology. Since the present modeling is fully local, the IBVP solution with damage effect is highly dependent on the mesh size inside the active zones. Thus, for 2D problems, an adaptive resolution methodology with mesh refinement and coarsening is used with various error indicators based either on thermomechanical fields as well as on the radius curvature of the contact interfaces [27,64,66]. In this adaptive resolution methodology, the lowest mesh size is naturally attributed to the fully damaged elements. However, for 3D calculations the mesh adaptation procedure is still under progress and the initial mesh is refined as required using the "convenient" mesh size obtained for a given material thanks to the identification procedure.

For the sake of shortness, all these numerical aspects are not detailed in the present paper. Instead, the reader is referred to the recent book [27] where all these numerical aspects are presented in details.

4. Application to sheet and bulk metal forming processes

To illustrate the predictive capacity of this numerical methodology, a few examples are now presented in what follows concerning both the sheet metal forming processes using the fully anisotropic model under isothermal room temperature conditions and the bulk metal forming processes using the fully isotropic model, but under anisothermal conditions.

All the numerical simulation in the sequel (Sections 4.1 and 4.3) are performed using the ABAQUS/Explicit based on the dynamic explicit resolution scheme to solve the IBVP together with the iterative fully implicit integration scheme to compute the stress tensor as well as the overall state variables at the end of each time increment.

4.1. Application to fully anisotropic and isothermal sheet metal forming

In this section, we will focus on the comparison of three different variants of the fully-coupled and fully anisotropic proposed model, through two examples of sheet metal forming at room temperature (i.e. under isothermal conditions): the bulge test with elliptical die (BTE) and the cross section deep drawing test (CSD). The three chosen variants of the anisotropic models are based on non-associative anisotropic elastoplasticity and differ mainly by the anisotropic character of the damage coupling. They are termed as following:

- Model 1: Plastic anisotropy with isotropic damage,
- Model 2: Plastic anisotropy with anisotropic ductile damage but without microcracks closure effect (i.e. $\hbar = 1$),
- Model 3: Plastic anisotropy with anisotropic ductile damage but with full microcracks closure effect (i.e. $\hbar = 0$).

These three variants are identified using the experimental results of X6CrNi18-09 stainless steel sheets given in [63]. Recall that this experimental database includes tensile tests at 0°, 45° and 90°, plane tension tests, cylindrical die bulge tests, and elliptical die bulge tests with 0°, 45° and 90° orientations of the elliptical major axis with respect to the material anisotropic directions. Only the last test (BTE), not used for the identification, is used to validate the model. Due to the fact that the three considered variants of the developed model differ only by the anisotropic character of ductile damage, hence all the variants will have the same elastoplastic identified material parameters summarized in Table 1. The damage parameters for each of the three variants are given in Table 2. Note that for these cases of local formulation, the smallest mesh size is fixed to $h_x = 0.5$ mm and this mesh size is conserved for all the sheet metal forming simulations with the same material.

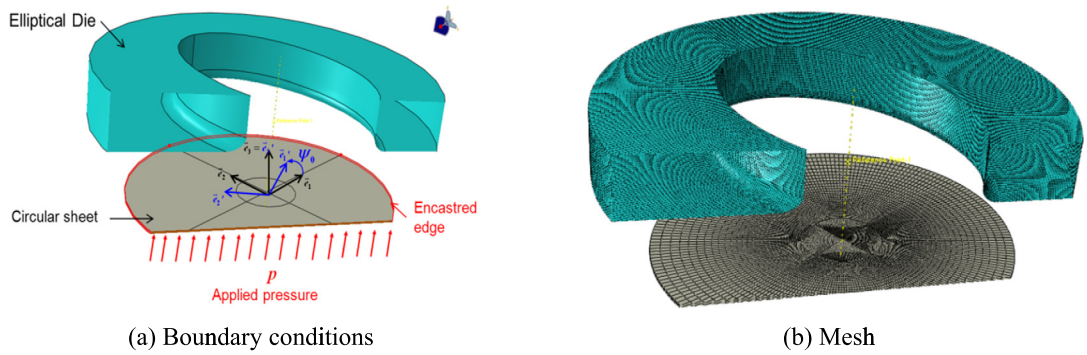

Fig. 2. The BTE model with the mesh and boundary conditions.

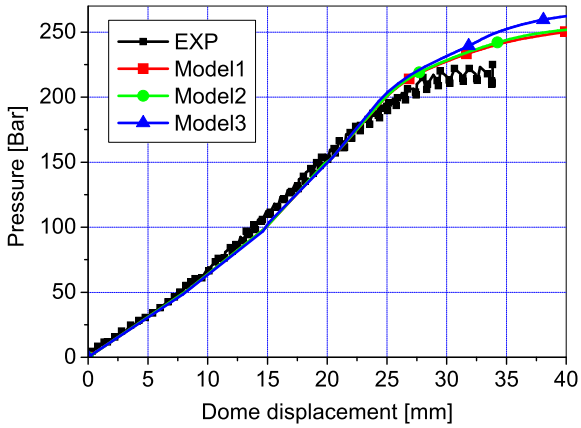

Fig. 3. Comparison between the experimental and numerically predicted results in terms of pressure versus displacement curves.

4.1.1. Bulge test with elliptical die (BTE)

This test schematized in Fig. 2 is widely used to characterize the formability of thin sheets. The die has elliptical shape with an external diameter $D_0 = 168$ mm, major axis $D_G = 110$ mm, minor axis $D_S = 74$ mm, and an edge radius $R = 6$ mm. The sheet has circular shape with uniform thickness $e = 1$ mm and external diameter $D = 133$ mm. The sheet is clamped on the die and an increasing internal pressure p is applied on the down face of the sheet while the displacement of the dome is measured continuously. The sheet is meshed with 156,328 hexahedral 8-nodes solid elements with reduced integration of type C3D8R (giving three element layers through thickness), and the die is supposed to be a rigid body meshed with 10,000 rigid elements of type R3D4, both taken from the ABAQUS® elements library.

With the use of an elliptical matrix we have the ability to deviate the loading path from equibiaxial to biaxial expansion according to the ratio of major by minor axes D_G/D_S of the elliptical die. This allows also studying the effect of the material orientation according to the major axis direction ψ_0. In this study, we limit ourselves to only two orientations $\psi_0 = 0°$ and $\psi_0 = 45°$. In our case, the ratio of in-plane major and minor strains $\varepsilon_{max}/\varepsilon_{min} = D_G/D_S = 1.5$. The global results, in terms of dome displacement vs applied pressure, have no significant difference for the three models, as shown in Fig. 3. We can observe good agreement with the experimental curve which is mainly due to a non-associative plasticity character, as discussed in detail in [63]. Note that these global results are not affected by the material orientation ψ_0.

Fig. 4 shows the numerically predicted damage maps obtained with the three models for both orientations (0° and 45°) at the macroscopic cracks initiation compared to the experimental one obtained for the case 45° (see Fig. 4d). By comparing these distributions to those corresponding to the initial orientation, we see a nearly insignificant effect of initial orientation on the initiation and propagation of macro-cracks for the various models.

On the other hand, it is found that all considered models predict the first crack initiation at the dome; however, every model predicts a different propagation path of the macro-cracks. It is also noted that the cracks propagate preferentially along the major axis of the ellipsoid mainly for the case of Model 3, as shown in Fig. 4c.

The predicted evolution of the anisotropic damage components at the dome (i.e. at the location of the first crack initiation) is given in Fig. 5. From this figure, significant differences in terms of plastic strain at the fracture are observed between Model 3 and the other two models. This is mainly due to the micro-cracks closure effect, which allows slower damage evolutions. It should be noted that for Model 2, the maximum damage component is given by the direction normal to the plane of the sheet (i.e. direction 3 in Fig. 2a), which is completely different from Model 3 for which the maximum component moving in the plane of the sheet (the plane (1 2)) and is carried by the direction normal to the minor ellipse

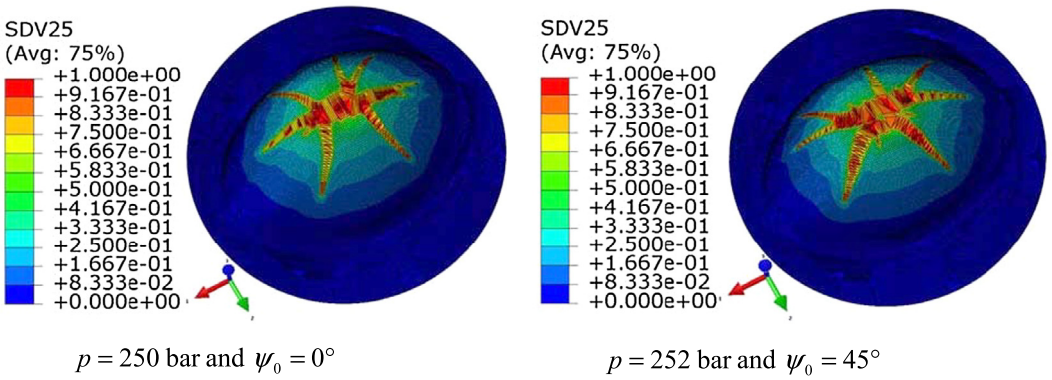

$p = 250$ bar and $\psi_0 = 0°$ $p = 252$ bar and $\psi_0 = 45°$

(a) Model 1

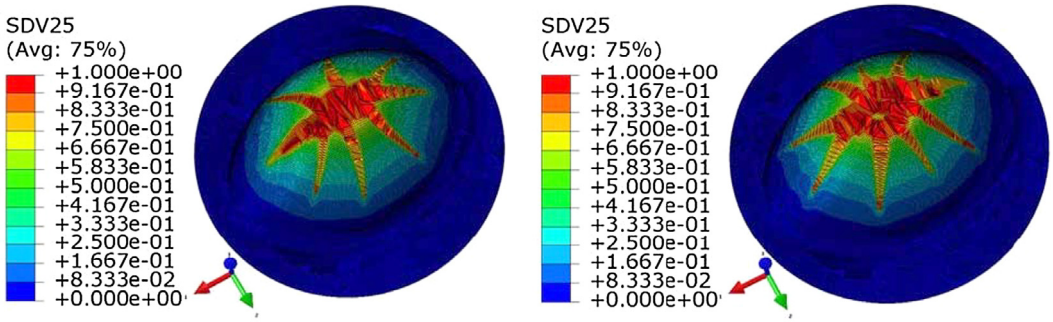

$p = 256$ bar and $\psi_0 = 0°$ $p = 257$ bar and $\psi_0 = 45°$

(b) Model 2

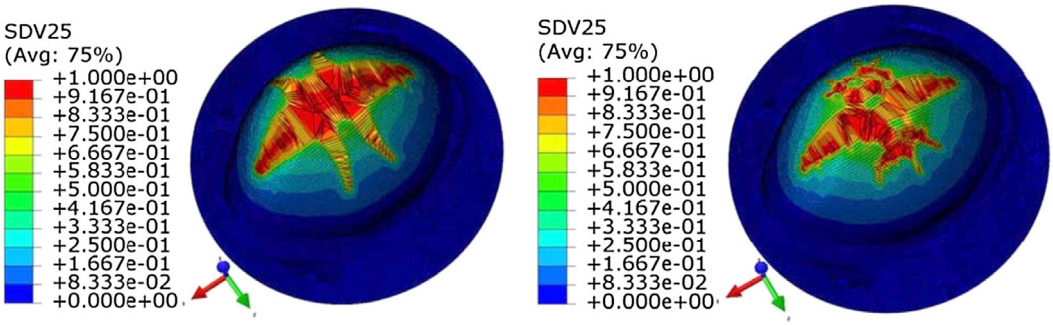

$p = 270$ bar and $\psi_0 = 0°$ $p = 272$ bar and $\psi_0 = 45°$

(c) Model 3

(d) Experimental failure for $\psi_0 = 45°$ and $p = 230$ bar.

Fig. 4. Comparison of the maximum damage maps obtained with the three models at the moment of the macro-cracks propagation for two different orientations $\psi_0 = 0°$ and $\psi_0 = 45°$.

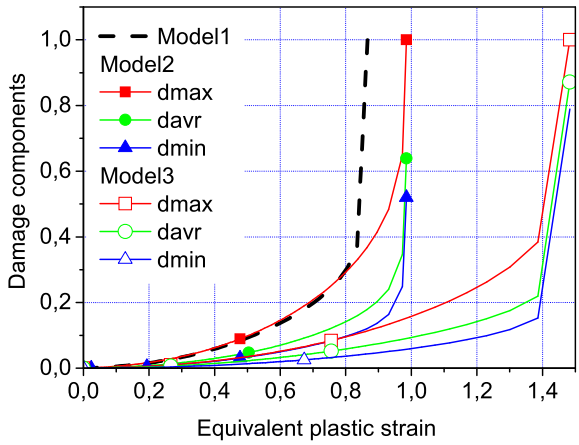

Fig. 5. Evolution of the local damage components (at the point located in the dome) obtained with the three models for $\psi_0 = 0°$.

axis (direction 2 in Fig. 2a). Note also that for model 3 the damage distribution is more localized in the direction of the die's major axis compared to the other models.

To analyze the crack path's orientation according to the used damage model, the plastic strain ratio $\varepsilon^{p}_{max}/\varepsilon^{p}_{min}$ and the maximum damage distributions along a circular area located at 30 mm from the dome are plotted in Fig. 6. These distributions are given for the maximum value of the ductile damage $d_{max} = 0.3$ reached at the dome. These figures reveal that plastic strain paths predicted by the three models vary considerably from 1.5 to 3, while browsing the circle from the point situated along direction 1. Note that the maximum strain ratio is obtained along the die's minor axis. However, the distribution of maximum damage follows the major axis direction of the elliptical die as shown in Fig. 6c and Fig. 6e.

4.2. Cross section deep drawing (SCD) test

In this process, the initial blank sheet has an octagonal shape, with length $L = 130$ mm and thickness $e = 1$ mm. This sheet is maintained between the die and the blank holder as shown in Fig. 7. The punch cross section has a flat bottom with a 200-mm major axis and a 140-mm minor axis. A force of 60 kN is applied on the blank holder in order to make easy the sheet swallowing. The meshing parameters of the different components of the SCD test are detailed in Fig. 7.

The contact between the blank and the various components is assumed to be of Coulomb type with the same constant friction coefficient $\mu = 0.17$ (with lubrication). The orientation of the punch with respect to the material anisotropic directions of the sheet, allows studying the off-axis loading paths. In this work, given the low plastic anisotropy and taking into account of the studies conducted in the previous section, this effect of this orientation will not be discussed.

In Fig. 8 are compared the responses in terms of global punch force–displacement curves for the three considered models. We note that both Model 1 and Model 2 predict almost the same maximum force (about 386 kN) and different failure displacements (49 mm for Model 1 and 56 mm for Model 2). However, Model 3 predicts higher maximum force (about 405 kN) and a larger displacement at fracture (about 70 mm) due to the lower increase of damage rate as expected.

The predicted distribution of the maximum damage values and the crack paths predicted by the three models are compared in Fig. 9. From this comparison the same critical area containing the first crack initiation and propagation, located at the corner in the side of major axis of the cross section punch, is observed. Consequently, the most important thickness reduction is located in this area. Note that, while Model 3 induces the more important failure punch displacement, it predicts the lower thickness reduction due to the lowest damage growth predicted by this model.

The damage state in the critical zone is also completely different, like in the previous example. Indeed, the maximum damage for Model 2 is carried out by the normal to the plane direction (i.e. direction 3); however, the maximum damage component for Model 3 is carried out by punch major axis.

4.3. Application to bulk metal forming

For the sake of shortness, only one example of bulk metal forming is presented. The proposed numerical methodology is now applied to an axisymmetric (2D) extrusion of a cold round billet schematized in Fig. 10a. In this figure, R_e is the initial radius of the billet, R_s is the final radius of the billet after extrusion, L the initial length of the billet, α is the semi-cone angle of the die, and $A_r = (R_e - R_s)/R_e$ is the radius reduction factor.

The good choices of the geometrical parameters (α and A_r), the friction condition, the material ductility and the temperature are essential to extrude a billet without defects. Unfavorable combinations of these parameters cause damage accumulation and chevron-shaped cracks located around the central axis (see Fig. 10b) or surface cracks located at the external surface of the billet (see Fig. 1c), which may result in final fracture of the extruded part during its use.

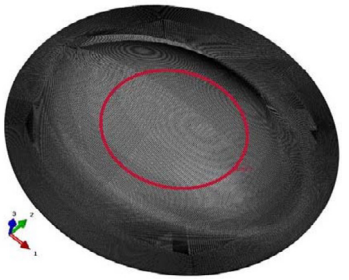

(a) Circular area surrounding the sheet dome.

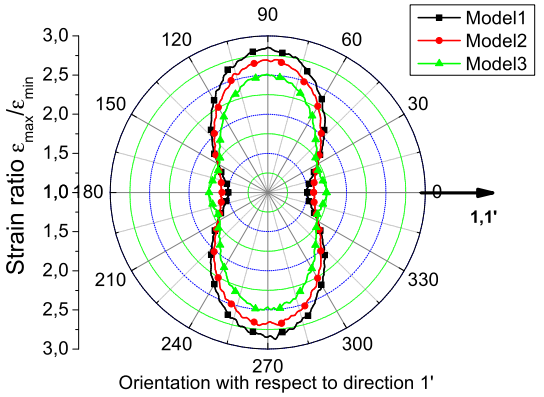

(b) Distributions of strain ratio $\varepsilon^{p}_{max} / \varepsilon^{p}_{min}$ with $\psi_0 = 0°$

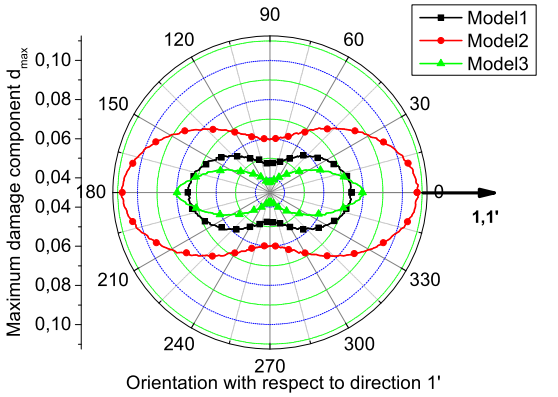

(c) Distributions maximum damage component d_{max} with $\psi_0 = 0°$

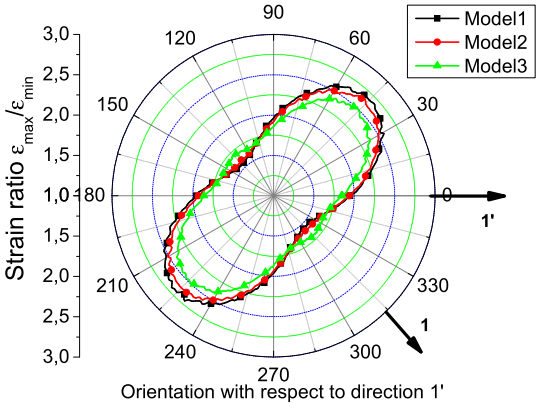

(d) Distributions of strain ratio $\varepsilon^{p}_{max} / \varepsilon^{p}_{min}$ with $\psi_0 = 45°$

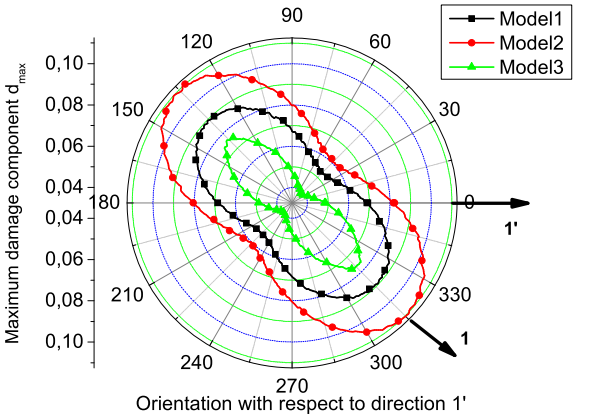

(e) Distributions maximum damage component d_{max} with $\psi_0 = 45°$

Fig. 6. Polar distribution of the plastic strain ratio $\varepsilon^{p}_{max}/\varepsilon^{p}_{min}$ and maximum damage along a circular neighborhood area located within a 30-mm radius from the dome.

The sample is taken from [59] using the same process parameters and the same material 100Cr6 steel. Due to the plastic isotropy of this material, only the model with isotropic plasticity fully coupled with isotropic ductile damage and the temperature is used. The geometrical parameters are: initial radius of the billet $R_e = 9.55$ mm, final radius $R_s = 7.5$ mm, die angle $\alpha = 45°$.

The moving punch moves with a constant speed of 5.0 mm/s. The billet is meshed with quadrangular axisymmetric element with reduced integration and thermal coupling (CAX4RT) of 0.2 mm × 0.2 mm dimension. The Coulomb friction model is used with $\mu = 0.04$, corresponding to coated contact condition. The tools are considered as rigid bodies. The initial temperature of the billet is $T_b = 25\,°C$.

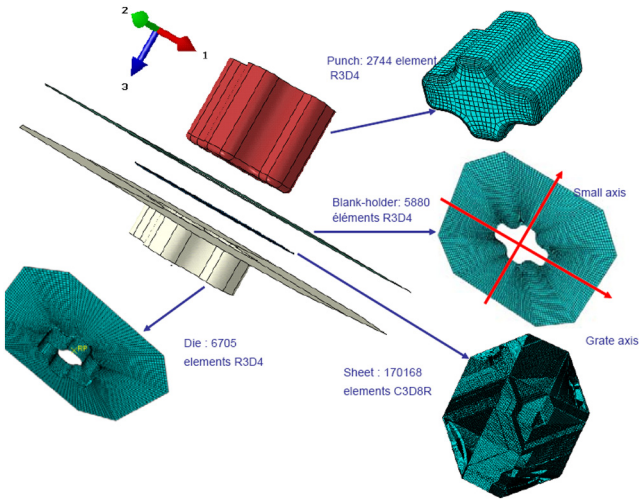

Fig. 7. Schematization of the CSD test.

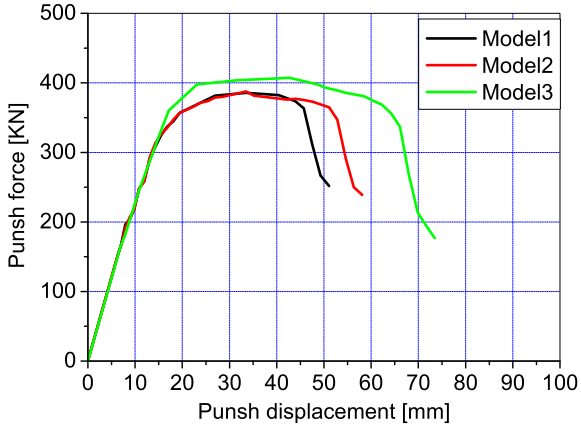

Fig. 8. Comparison of global force–displacement curves predicted by the three models for a SDC test.

The material's behavior is taken fully isotropic thermo-elasto-viscoplastic fully coupled with thermal effect. The parameters of the material corresponding to 100Cr6 steel is based on the experimental results taken from [59,74]. The different materials and thermal parameters are given in Table 3.

The numerical simulation is performed with ABAQUS/Explicit using the VUMAT together with fully adaptive 2D methodology [66,74]. The obtained results are presented in the following figures.

At the end of the extrusion operation, several chevron-shaped cracks inside the billet are predicted, as shown by Fig. 11 where the distribution of the equivalent von Mises stress and the temperature are presented. From Fig. 11a it is clearly observed that the stress concentration is located in the reduction zone between the die and the billet with a maximum value of 1011 MPa, while the stresses are zero inside the chevron-shaped cracks according to the full coupling between the damage and the behavior. The temperature distribution is shown in Fig. 11b, where it is varying between a maximum of 251 °C located at the same reduction zone between the die and the billet, and a minimum of 25 °C. The increase of the temperature is expected to be generated by inelastic work and the friction at the contact interface.

Fig. 12 shows the distribution of the accumulated plastic strain after a 40 mm punch displacement; five chevron-shaped cracks are predicted by the model, which compares very well with the experimental result [59].

The evolution of the punch force versus the displacement of the punch is plotted in Fig. 13. It increases rapidly to reach 250 kN and then oscillates around this value as the chevron-shaped cracks are initiated. The number of the force peaks corresponds to the number of chevron-shaped cracks and the oscillation of the punch force indicates the presence of these discontinuous chevron-shaped cracks.

The Zimmerman diagram [111,112] plotted for two different values of the Coulomb friction parameter μ is given in Fig. 14.

This diagram consists in the curves indicating the formation of the chevron-shaped cracks and the surface cracks for different simulations performed with different values of the couple (α, Ar), as indicated in Fig. 14. The domain Ω_c of

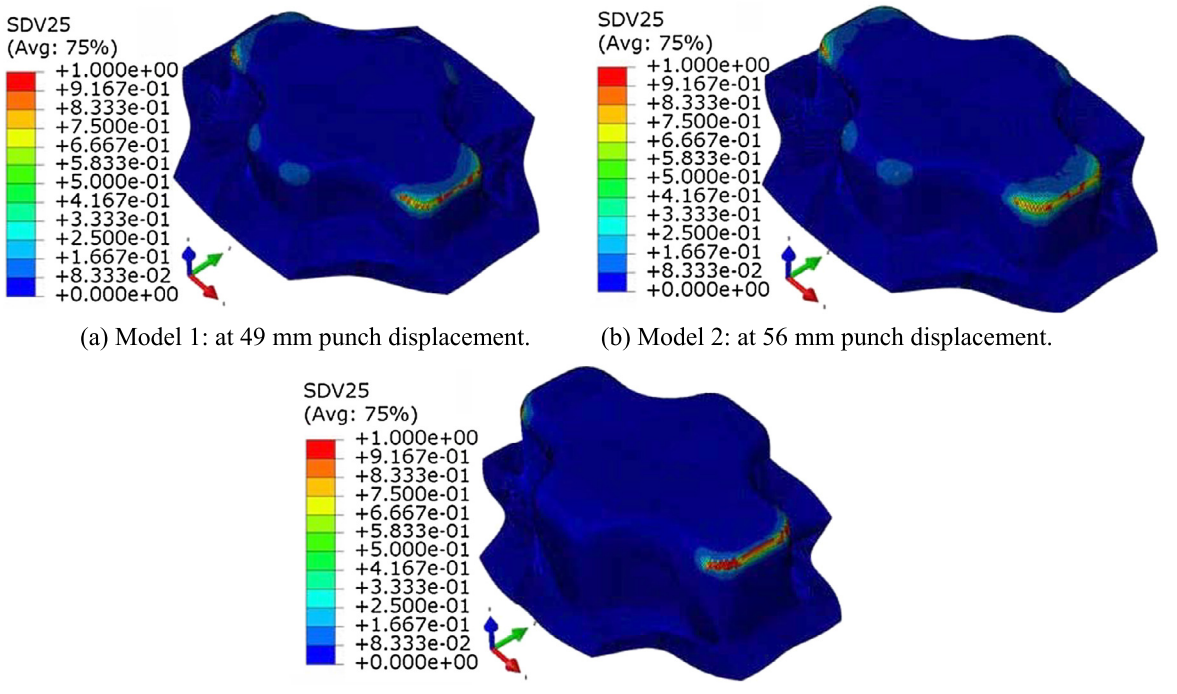

(a) Model 1: at 49 mm punch displacement.

(b) Model 2: at 56 mm punch displacement.

(c) Model 3 with: at 71 mm punch displacement.

Fig. 9. Comparison of the maximum damage maps obtained with the three models (zones where $D = 1$ defines the location of the macroscopic cracks).

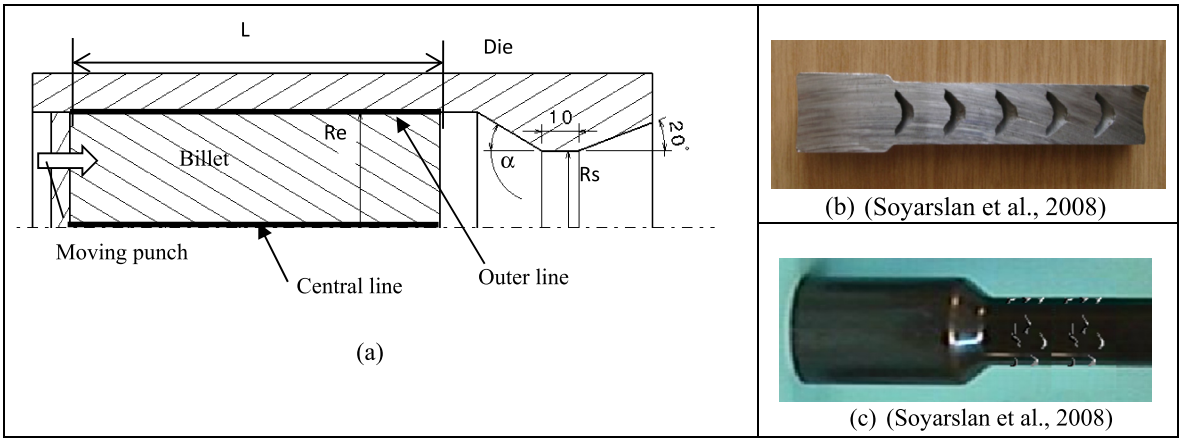

Fig. 10. a) Schematic representation of the extrusion process, b) chevron-shaped cracks, c) external surface cracks.

Chevron-shaped cracks is indicated by the red line, while the domain Ω_s of external surface cracks is delimited by the green line. The safe domain Ω_{safe} is given by $\Omega_{safe} = \Omega - \Omega_c \cup \Omega_s$. As clearly shown by Fig. 11, the delimitation of the safe domain depends highly on the friction condition at the contact interfaces:

- for the Coulomb friction parameter $\mu = 0.05$, the chevron-shaped crack appears for a radius reduction superior to 10%. Some defects can also appear in the external surface of the billet, but for large values of A_r and α,
- for the coulomb friction parameter $\mu = 0.1$, the domain of external surface defect Ω_s increases at the expense of the chevron-shaped crack domain. Indeed, when the outer surface of the billet is too damaged, the internal forces are no longer transmitted to the center of the billet, avoiding the formation of chevron-shaped cracks.

5. Conclusion and main perspectives

The main objective of this paper is to show the high predictive capability of the proposed 3D numerical methodology in the simulation of various, sheet and bulk metal forming, processes. This methodology is based on advanced “strongly”

Table 3
Thermo-elasto-viscoplastic properties of the material.

E (GPa)	ν	C_ϵ ($J{\cdot}kg^{-1}{\cdot}C^{-1}$)	k_0 ($W{\cdot}m^{-1}{\cdot}C^{-1}$)	α_t (C^{-1})	T_0 (°C)	T_f (°C)	Thermal functions
205	0.28	475	32	$1.2e^{-6}$	25	1520	$Z(T) = 1 - (\frac{T-T_0}{T_f-T_0})^{1.3}$

Viscoplastic, hardening and ductile damage properties:

K_v (MPa)	n_v	σ_y (MPa)	Q (MPa)	b	C (MPa)	a	S	s	β	Y_0	γ	$\hbar$	h_x (mm)
100 Z(T)	10	650 Z(T)	720 Z(T)	30	200 Z(T)	30	3.8 Z(T)	1.2	1	0.	6	0	0.2

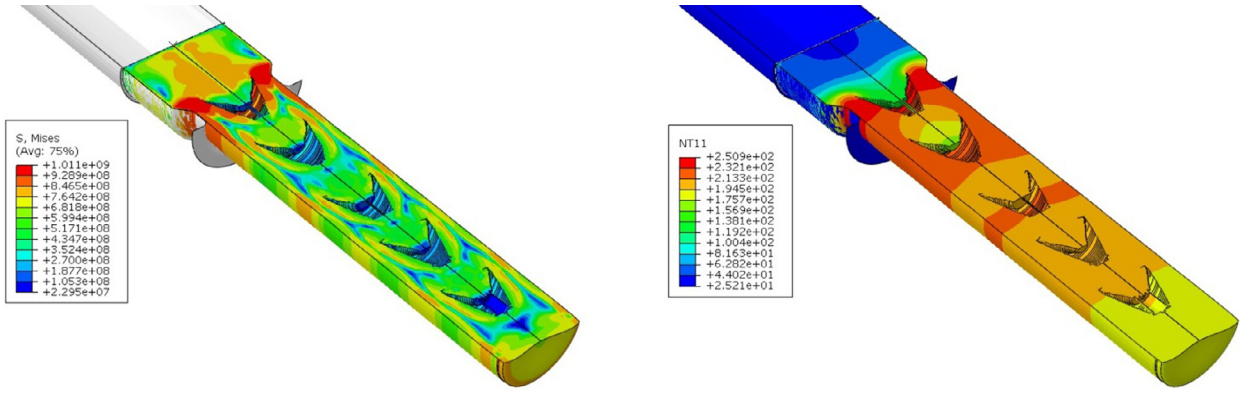

(a) von Mises stress (N/m^2) distribution (b) Temperature (°C) distribution

Fig. 11. von Mises stress (N/m^2) distribution.

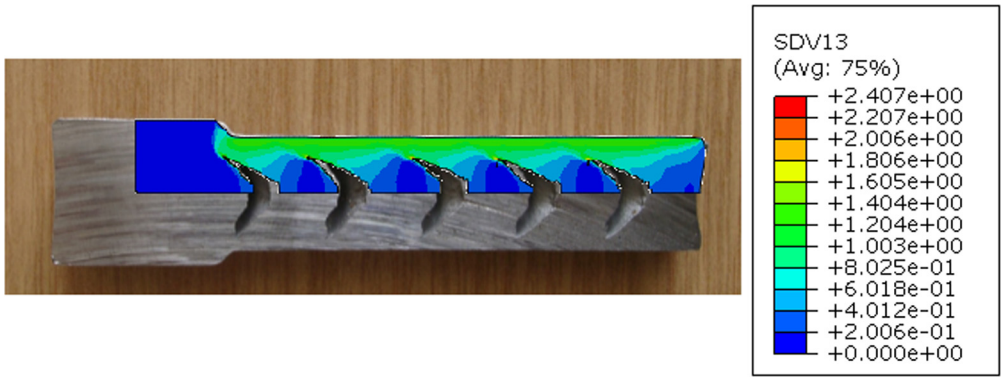

Fig. 12. Comparison of the experimental and predicted chevron cracks after 40-mm punch displacement.

coupled constitutive equations accounting for various thermomechanical phenomena as thermal, “small” elastic strains, large inelastic (plastic or viscoplastic) strains, ductile isotropic and/or anisotropic damage …

This kind of numerical methodology can be helpfully used to optimize any forming or machining process in order to determine the best forming or machining plan that minimizes the undesirable defects under a low economical cost and a low carbon emission according to the demand of the new environmental requirements. Accordingly, using highly predictive constitutive equations representing the ‘realistic’ physical phenomena and their mutual interactions (or strong coupling) allows one to:

- minimize the occurrence of ductile damage in formed parts in order to obtain safe components without any defects (i.e. cracks, localization zones, wrinkles zones, etc.) as in deep drawing of thin sheets, hydroforming of tubes or sheets hot or cold forging or extrusion,
- maximize the occurrence of ductile damage in formed parts by controlling its intensity and direction to reproduce various material cutting operations such as stamping of thin or thick parts by sheering, or slitting and guillotining thin sheets or machining by chip formation and segmentation

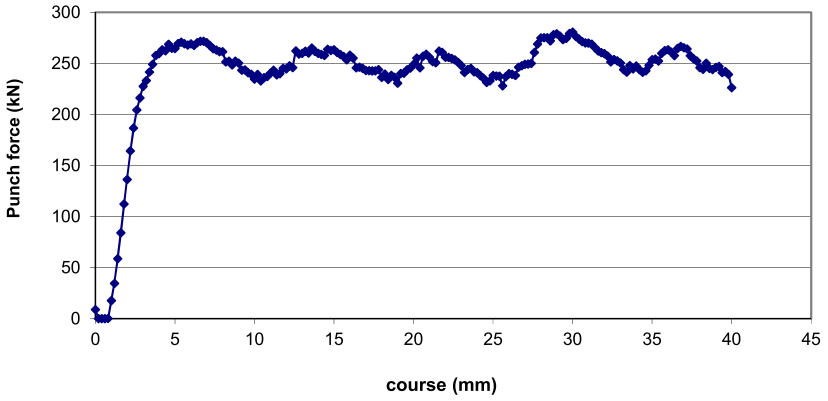

Fig. 13. Punch force versus Punch course.

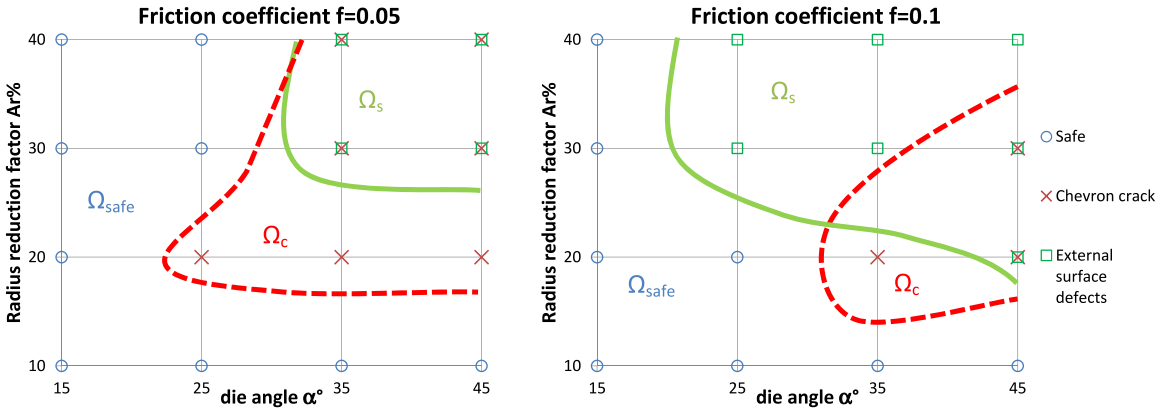

Fig. 14. The Zimmerman diagram for the axisymmetric extrusion process.

- minimize various kinds of damage (wear, friction, cracks, etc.) inside forming tools (matrices, dies, cutting tools...) and at the metal/tool contact interfaces in order to increase their life.

However, all the models presented in this paper are obtained from fully local formulations for which the kinematics and the behavior of the continuum are fully determined by the knowledge of the first gradient of the displacement field known as the Cauchy continuum. It is well established that, for this kind of local constitutive equations, the strong coupling with damage leads damage-induced softening. This makes the solution of the IBVP highly dependent on the discretization of the time domain and of the space domain. This problem has been approximately solved here by imposing a convenient mesh size and time step size for each material, determined during the identification procedure.

In fact, an elegant solution to this problem can be obtained from the generalized continua as the micromorphic theory [27,113–118] in which:

- the kinematics of the homogeneous transformation is enriched by adding new micromorphic degrees of freedom. The application of the principle of the virtual power leads to obtaining the classical equilibrium equations and additional balance equations with their Neumann boundary conditions related to the targeted micromorphic phenomena;
- the space of the state variables is extended by adding new micromorphic state variables. Accordingly, the use of the classical thermodynamics of irreversible processes allows obtaining state relations and evolution equations deduced from adequate state potential and dissipation potentials.

The application of these generalized micromorphic constitutive equation to metal forming simulation will be addressed in a forthcoming paper.

References

[1] Z. Marciniak, K. Kuczyński, Limit strain in the processes of stretch forming sheet steel, J. Mech. Phys. Solids 1 (1967) 609–620.
[2] Z. Marciniak, K. Kuczyński, T. Pokora, Influence of the plastic properties of a material on the forming limit diagram for sheet metal in tension, Int. J. Mech. Sci. 15 (1973) 789–800.

[3] A.K. Ghosh, J.V. Laukonis, Influence of strain-path changes on the formability of sheet steel, in: SMFaE Conversion, ASM (Ed.), Metals Park, Ohio, 1977, pp. 167–178.
[4] R. Arrieux, C. Bedrin, M. Boivin, Determination of an intrinsic forming limit stress diagram for isotropic sheets, in: Proceedings of the 12th IDDRG Congress, 1982, pp. 61–71.
[5] R. Arrieux, M. Boivin, F. Le Maître, Determination of the forming limit stress curve for anisotropic sheets, CIRP Ann. 36 (1987) 195–198.
[6] A.F. Graf, W.F. Hosford, Calculations of forming limit, Metall. Trans. A, Phys. Metall. Mater. Sci. 24 (1993) 2497–2501.
[7] R. Arrieux, Determination and use of the forming limit stress diagrams in sheet metal forming, J. Mater. Process. Technol. 53 (1995) 47–56.
[8] T.B. Stoughton, Stress-based forming limits in sheet-metal forming, J. Eng. Mater. Technol. 123 (2001) 417–422.
[9] P. Matin, L. Smith, S. Petrusevski, A method for stress space forming limit diagram construction for aluminum alloys, J. Mater. Process. Technol. 174 (2006) 258–265.
[10] A. Assempour, R. Hashemi, K. Abrinia, M. Ganjiani, E. Masoumi, A methodology for prediction of forming limit stress diagrams considering the strain path effect, Comput. Mater. Sci. 45 (2009) 195–204.
[11] W. Chien, J. Pan, S. Tang, A combined necking and shear localization analysis for aluminum sheets under biaxial stretching conditions, Int. J. Plast. 20 (2004) 1953–1981.
[12] M. Yoshida, F. Yoshida, H. Konishi, K. Fukumoto, Fracture limits of sheet metals under stretch bending, Int. J. Mech. Sci. 47 (2005) 1885–1896.
[13] K. Yoshida, T. Kuwabara, Effect of strain hardening behavior on forming limit stresses of steel tube subjected to nonproportional loading paths, Int. J. Plast. 23 (2007) 1260–1284.
[14] P. Hora, L. Tong, Prediction of failure under complex 3D-stress conditions, in: Proceedings of Forming Technology Forum 2009, ETH Zurich, IVP, 2009, pp. 133–138.
[15] J. Carbonniere, S. Thuillier, F. Sabourin, M. Brunet, P.-Y. Manach, Comparison of the work hardening of metallic sheets in bending–unbending and simple shear, Int. J. Mech. Sci. 51 (2009) 122–130.
[16] N. Le Maoût, S. Thuillier, P.-Y. Manach, Aluminum alloy damage evolution for different strain paths—application to hemming process, Eng. Fract. Mech. 76 (2009) 1202–1214.
[17] P. Hora, L. Tong, Prediction of failure under complex 3D-stress conditions, in: Proceedings of Forming Technology Forum 2009, 5–6 May, IVP, ETH Zurich, 2009, pp. 133–138.
[18] H.W. Swift, Plastic instability under plane stress, J. Mech. Phys. Solids 1 (1952) 1–18.
[19] S. Stören, J. Rice, Localized necking in thin sheets, J. Mech. Phys. Solids 23 (1975) 421–441.
[20] J. Bressan, J. Williams, The use of a shear instability criterion to predict local necking in sheet metal deformation, Int. J. Mech. Sci. 25 (1983) 155–168.
[21] A. Needleman, N. Triantafyllidis, Void growth and local necking in biaxially stretched sheets, J. Eng. Mater. Technol. 100 (1978) 164–169.
[22] C.-C. Chu, An analysis of localized necking in punch stretching, Int. J. Solids Struct. 16 (1980) 913–931.
[23] C. Chu, A. Needleman, Void nucleation effects in biaxially stretched sheets, J. Eng. Mater. Technol. 102 (1980) 249–256.
[24] M. Brunet, F. Morestin, Experimental and analytical necking studies of anisotropic sheet metals, J. Mater. Process. Technol. 112 (2001) 214–226.
[25] P.M. Dixit, U.S. Dixit, Modeling of Metal Forming and Machining Processes: By Finite Element and Soft Computing Methods, Springer Science & Business Media, 2008.
[26] K. Saanouni, Modélisation et simulation numériques en formage virtuel, Lavoisier, 2012.
[27] K. Saanouni, Damage Mechanics in Metal Forming: Advanced Modeling and Numerical Simulation, John Wiley & Sons, 2012.
[28] J. Gelin, J. Oudin, Y. Ravalard, A. Moisan, An improved finite element method for the analysis of damage and ductile fracture in cold forming processes, CIRP Ann. 34 (1985) 209–213.
[29] L. Hao, P. Ke, W. June, An anisotropic damage criterion for deformation instability and its application to forming limit analysis of metal plates, Eng. Fract. Mech. 21 (1985) 1031–1054.
[30] K. Mathur, P. Dawson, Damage evolution modeling in bulk forming processes, in: Computational Methods for Predicting Material Processing Defects, 1987, pp. 251–262.
[31] E. Onate, M. Kleiber, D. Saracibar, C. Agelet, Plastic and viscoplastic flow of void-containing metals: applications to axisymmetric sheet forming problems, Int. J. Numer. Methods Eng. 25 (1988) 227–251.
[32] P. Hartley, S.E. Clift, J. Saliminamin, C. Sturgess, I. Pillinger, The prediction of ductile fracture initiation in metalforming using a finite-element method and various fracture criteria, Res. Mech. 28 (1989) 269–293.
[33] J. Gelin, A. Moisan, Finite element analysis of ductile fracture and defects formation in cold and hot forging, CIRP Ann. 39 (1990) 215–218.
[34] N. Bontcheva, R. Iankov, Numerical investigation of the damage process in metal forming, Eng. Fract. Mech. 40 (1991) 387–393.
[35] Y. Zhu, S. Cescotto, The finite element prediction of ductile fracture initiation in dynamic metalforming processes, J. Phys. IV 1 (1991), C3-751–C753-757.
[36] M. Brunet, F. Sabourin, S. Mguil-Touchal, The prediction of necking and failure in 3 D: sheet forming analysis using damage variable, J. Phys. IV 6 (1996), C6-473–C476-482.
[37] M. Brunet, F. Morestin, H. Walter-Leberre, Failure analysis of anisotropic sheet-metals using a non-local plastic damage model, J. Mater. Process. Technol. 170 (2005) 457–470.
[38] Y. Zhu, S. Cescotto, A. Habraken, A fully coupled elastoplastic damage modeling and fracture criteria in metalforming processes, J. Mater. Process. Technol. 32 (1992) 197–204.
[39] Y. Zhu, S. Cescotto, A fully coupled elasto-visco-plastic damage theory for anisotropic materials, Int. J. Solids Struct. 32 (1995) 1607–1641.
[40] K. Saanouni, K. Nesnas, Y. Hammi, Damage modeling in metal forming processes, Int. J. Damage Mech. 9 (2000) 196–240.
[41] K. Saanouni, Y. Hammi, Numerical Simulation of Damage in Metal Forming Processes, Elsevier, New York, 2000.
[42] K. Saanouni, A. Cherouat, Y. Hammi, Numerical aspects of finite elastoplasticity with isotropic ductile damage for metal forming, Rev. Eur. Éléments Finis 2-3-4 (2001) 327–351.
[43] K. Saanouni, A. Cherouat, Y. Hammi, Numerical aspects of finite elastoplasticity with damage for metal forming, Rev. Eur. Éléments Finis 10 (2001) 4.
[44] P. Villon, H. Borouchaki, K. Saanouni, Transfert de champs plastiquement admissibles, C. R. Mecanique 330 (2002) 313–318.
[45] A. Cherouat, K. Saanouni, Y. Hammi, Numerical improvement of thin tubes hydroforming with respect to ductile damage, Int. J. Mech. Sci. 44 (2002) 2427–2446.
[46] A. Cherouat, K. Saanouni, Y. Hammi, Improvement of forging process of a 3D complex part with respect to damage occurrence, J. Mater. Process. Technol. 142 (2003) 307–317.
[47] A. Cherouat, K. Saanouni, Numerical simulation of sheet metal blanking process using a coupled finite elastoplastic damage modelling, Int. J. Form. Process. 6 (2003) 7–32.
[48] K. Saanouni, J.L. Chaboche, Computational damage mechanics: application to metal forming simulation, in: I. Milne, R.O. Ritchie, B. Karihaloo (Eds.), Comprehensive Structural Integrity, Pergamon, Oxford, 2003, pp. 321–376.
[49] P. Lestriez, K. Saanouni, J.-F. Mariage, A. Cherouat, Numerical prediction of ductile damage in metal forming processes including thermal effects, Int. J. Damage Mech. 13 (2004) 59–80.
[50] K. Saanouni, J. Mariage, A. Cherouat, P. Lestriez, Numerical prediction of discontinuous central bursting in axisymmetric forward extrusion by continuum damage mechanics, Comput. Struct. 82 (2004) 2309–2332.

[51] J. Mariage, K. Saanouni, P. Lestriez, A. Cherouat, Numerical simulation of an hexnut forming process including damage effect, Int. J. Form. Process. 8 (2005) 291.
[52] P. Lestriez, K. Saanouni, A. Cherouat, Simulation numérique de la coupe orthogonale par couplage thermique–comportement–endommagement en transformations finies, Méc. Ind. 6 (2005) 297–307.
[53] K. Saanouni, Virtual metal forming including the ductile damage occurrence: actual state of the art and main perspectives, J. Mater. Process. Technol. 177 (2006) 19–25.
[54] J. Chaboche, M. Boudifa, K. Saanouni, A CDM approach of ductile damage with plastic compressibility, Int. J. Fract. 137 (2006) 51–75.
[55] J.C. de Sá, P. Areias, C. Zheng, Damage modelling in metal forming problems using an implicit non-local gradient model, Comput. Methods Appl. Mech. Eng. 195 (2006) 6646–6660.
[56] H. Badreddine, K. Saanouni, A. Dogui, M. Amen Gahbich, Elastoplasticité anisotrope non normale en grandes deformations avec endommagement: application à la mise en forme des tôles minces, Eur. J. Comput. Mech. 16 (2007) 913–940.
[57] K. Saanouni, On the numerical prediction of the ductile fracture in metal forming, Eng. Fract. Mech. 75 (2008) 3545–3559.
[58] K. Saanouni, H. Badreddine, M. Ajmal, Advances in virtual metal forming including the ductile damage occurrence: application to 3D sheet metal deep drawing, J. Eng. Mater. Technol. 130 (2008) 02102201–02102211.
[59] C. Soyarslan, A.E. Tekkaya, U. Akyuz, Application of continuum damage mechanics in discontinuous crack formation: forward extrusion chevron predictions, Z. Angew. Math. Mech. 88 (2008) 436–453.
[60] M. Boudifa, K. Saanouni, J.-L. Chaboche, A micromechanical model for inelastic ductile damage prediction in polycrystalline metals for metal forming, Int. J. Mech. Sci. 51 (2009) 453–464.
[61] K. Saanouni, N. Belamri, P. Autesserre, Finite element simulation of 3D sheet metal guillotining using advanced fully coupled elastoplastic–damage constitutive equations, Finite Elem. Anal. Des. 46 (2010) 535–550.
[62] K. Saanouni, P. Lestriez, Modelling and numerical simulation of ductile damage in bulk metal forming, Steel Res. Int. 80 (2009) 645–657.
[63] H. Badreddine, K. Saanouni, A. Dogui, On non-associative anisotropic finite plasticity fully coupled with isotropic ductile damage for metal forming, Int. J. Plast. 26 (2010) 1541–1575.
[64] M. Issa, C. Labergère, K. Saanouni, A. Rassineux, Numerical prediction of thermomechanical field localization in orthogonal cutting, CIRP J. Manuf. Sci. Technol. 5 (2012) 175–195.
[65] K. Saanouni, P. Lestriez, C. Labergère, 2D adaptive FE simulations in finite thermo-elasto-viscoplasticity with ductile damage: application to orthogonal metal cutting by chip formation and breaking, Int. J. Damage Mech. 20 (2011) 23–61.
[66] C. Labergère, A.A. Rassineux, K.K. Saanouni, 2D adaptive mesh methodology for the simulation of metal forming processes with damage, Int. J. Mater. Forming 4 (2011) 317–328.
[67] D. Sornin, K. Saanouni, About elastoplastic nonlocal formulations with damage gradients, Int. J. Damage Mech. 20 (2011) 845–875.
[68] Z. Yue, C. Soyarslan, H. Badreddine, K. Saanouni, A. Tekkaya, Identification of fully coupled anisotropic plasticity and damage constitutive equations using a hybrid experimental–numerical methodology with various triaxialities, Int. J. Damage Mech. (2014).
[69] H. Badreddine, K. Saanouni, T.D. Nguyen, Damage anisotropy and its effect on the plastic anisotropy evolution under finite strains, Int. J. Solids Struct. 63 (2015) 11–31.
[70] Z. Yue, H. Badreddine, T. Dang, K. Saanouni, A. Tekkaya, Formability prediction of AL7020 with experimental and numerical failure criteria, J. Mater. Process. Technol. 218 (2015) 80–88.
[71] S. Msolli, H. Badreddine, C. Labergere, M. Martiny, G. Robin, M. Jrad, K. Saanouni, F. Choquart, Experimental characterization and numerical prediction of ductile damage in forming of AA1050-O sheets, Int. J. Mech. Sci. 99 (2015) 262–273.
[72] K. Saanouni, C. Forster, F.B. Hatira, On the anelastic flow with damage, Int. J. Damage Mech. 3 (1994) 140–169.
[73] J. Lemaitre, A Course on Damage Mechanics, Springer-Verlag, Berlin, 1992.
[74] C. Labergere, A. Rassineux, K. Saanouni, Numerical simulation of continuous damage and fracture in metal forming processes with 2D mesh adaptive methodology, Finite Elem. Anal. Des. 82 (2014) 46–61.
[75] M. Brünig, Numerical analysis and elastic–plastic deformation behavior of anisotropically damaged solids, Int. J. Plast. 18 (2002) 1237–1270.
[76] M. Brünig, An anisotropic ductile damage model based on irreversible thermodynamics, Int. J. Plast. 19 (2003) 1679–1713.
[77] S. Murakami, N. Ohno, A continuum theory of creep and creep damage, in: Creep in Structures, Springer, 1981, pp. 422–444.
[78] S. Murakami, M. Kawai, H. Rong, Anisotropic damage theory and its application to creep crack growth analysis, J. Soc. Mater. Sci. Jpn. 37 (1988) 278–282.
[79] S. Murakami, Continuum Damage Mechanics: A Continuum Mechanics Approach to the Analysis of Damage and Fracture, vol. 185, Springer Science & Business Media, 2012.
[80] J. Cordebois, F. Sidoroff, Anisotropic damage in elasticity and plasticity, J. Méc. Théor. Appl. (1982) 45–60.
[81] J. Cordebois, F. Sidoroff, Anisotropie élastique induite par endommagement, in: Comportement mécanique des solides anisotropes, 1979, pp. 761–774.
[82] J. Betten, Applications of tensor functions to the formulation of constitutive equations involving damage and initial anisotropy, Eng. Fract. Mech. 25 (1986) 573–584.
[83] J.-L. Chaboche, Damage induced anisotropy: on the difficulties associated with the active/passive unilateral condition, Int. J. Damage Mech. 1 (1992) 148–171.
[84] J.-L. Chaboche, Development of continuum damage mechanics for elastic solids sustaining anisotropic and unilateral damage, Int. J. Damage Mech. 2 (1993) 311–329.
[85] N. Hansen, H. Schreyer, A thermodynamically consistent framework for theories of elastoplasticity coupled with damage, Int. J. Solids Struct. 31 (1994) 359–389.
[86] G.Z. Voyiadjis, P.I. Kattan, A plasticity–damage theory for large deformation of solids, I: theoretical formulation, Int. J. Eng. Sci. 30 (1992) 1089–1108.
[87] G.Z. Voyiadjis, P.I. Kattan, Finite strain plasticity and damage in constitutive modeling of metals with spin tensors, Appl. Mech. Rev. 45 (1992) S95–S109.
[88] G.Z. Voyiadjis, Z.N. Taqieddin, P.I. Kattan, Theoretical formulation of a coupled elastic–plastic anisotropic damage model for concrete using the strain energy equivalence concept, Int. J. Damage Mech. (2009).
[89] G.Z. Voyiadjis, Advances in Damage Mechanics: Metals and Metal Matrix Composites, Elsevier, 2012.
[90] W. Rajhi, K. Saanouni, H. Sidhom, Anisotropic ductile damage effects on anisotropic plastic flow: modeling, numerical simulation and experimental validation, Int. J. Damage Mech. 23 (2014) 1211–1256.
[91] C. Chow, T. Lu, On evolution laws of anisotropic damage, Eng. Fract. Mech. 34 (1989) 679–701.
[92] J. Lemaitre, R. Desmorat, M. Sauzay, Anisotropic damage law of evolution, Eur. J. Mech. A, Solids 19 (2000) 187–208.
[93] J. Lemaitre, R. Desmorat, Engineering Damage Mechanics: Ductile, Creep, Fatigue and Brittle Failures, Springer Science & Business Media, 2005.
[94] C. Chow, J. Wang, An anisotropic theory of continuum damage mechanics for ductile fracture, Eng. Fract. Mech. 27 (1987) 547–558.
[95] P. Germain, Q.S. Nguyen, P. Suquet, Continuum thermodynamics, J. Appl. Mech. 50 (1983) 1010–1020.
[96] J. Marigo, Modelling of brittle and fatigue damage for elastic material by growth of microvoids, Eng. Fract. Mech. 21 (1985) 861–874.
[97] M. Ortiz, A constitutive theory for the inelastic behavior of concrete, Mech. Mater. 4 (1985) 67–93.

[98] J. Mazars, A model of unilateral elastic damageable material and its application to concrete, in: Fracture Toughness and Fracture Energy of Concrete, Elsevier, New York, 1986.
[99] J. Ju, On energy-based coupled elastoplastic damage theories: constitutive modeling and computational aspects, Int. J. Solids Struct. 25 (1989) 803–833.
[100] J. Mazars, Y. Berthaud, S. Ramtani, The unilateral behaviour of damaged concrete, Eng. Fract. Mech. 35 (1990) 629–635.
[101] J. Chaboche, P. Lesne, J. Maire, Continuum damage mechanics, anisotropy and damage deactivation for brittle materials like concrete and ceramic composites, 1995.
[102] J. Lemaitre, J.-L. Chaboche, A. Benallal, R. Desmorat, Mécanique des matériaux solides, 3ème éditions, Dunod, Paris, 2009.
[103] R. Desmorat, Quasi-unilateral conditions in anisotropic elasticity, C. R. Acad. Sci., Sér. 2, Méc. Phys. Chim. Astron. 328 (2000) 445–450.
[104] R. Desmorat, S. Cantournet, Modeling microdefects closure effect with isotropic/anisotropic damage, Int. J. Damage Mech. (2007).
[105] P. Ladevèze, On an anisotropic damage theory, in: J.P. Boehler (Ed.), Failure Criteria of Structured Media, Balkema, Rotterdam, 1993, pp. 355–363.
[106] T.J. Hughes, The Finite Element Method: Linear Static and Dynamic Finite Element Analysis, Courier Corporation, 2012.
[107] K.J. Bathe, Finite Element Procedures, Prentice Hall, Upper Saddle River, 1996.
[108] T. Belytschko, W.K. Liu, B. Moran, Nonlinear Finite Elements for Continua and Structures, Wiley, 2000.
[109] J.C. Simo, T.J.R. Hughes, Computational Inelasticity, Springer-Verlag Inc., New York, 1998.
[110] E.A. de Souza Neto, D. Peric, D.R.J. Owen, Computational Methods for Plasticity: Theory and Applications, John Wiley & Sons, 2011.
[111] Z. Zimerman, B. Avitzur, Analysis of the effect of strain hardening on central bursting defects in drawing and extrusion, J. Eng. Ind. 92 (1970) 135–145.
[112] N. Aravas, The analysis of void growth that leads to central bursts during extrusion, J. Mech. Phys. Solids 34 (1986) 55–79.
[113] A.C. Eringen, Microcontinuum Field Theories, I: Foundations and Solids, Springer Verlag, New York, 1999.
[114] A.C. Eringen, Nonlocal Continuum Field Theories, Springer Science & Business Media, 2002.
[115] S. Forest, R. Sievert, Elastoviscoplastic constitutive frameworks for generalized continua, Acta Mech. 160 (2003) 71–111.
[116] S. Forest, Milieux continus généralisés et matériaux hétérogènes, Presses des MINES, 2006.
[117] S. Forest, Micromorphic approach for gradient elasticity, viscoplasticity, and damage, J. Eng. Mech. 135 (2009) 117–131.
[118] K. Saanouni, M. Hamed, Micromorphic approach for finite gradient-elastoplasticity fully coupled with ductile damage: formulation and computational aspects, Int. J. Solids Struct. 50 (2013) 2289–2309.